

# A probabilistic elasticity model for long fiber reinforced thermoplastics with uncertain microstructure

Jörg Hohe\*, Hanna Paul†, Carla Beckmann

Fraunhofer-Institut für Werkstoffmechanik IWM  
Wöhlerstr. 11, 79108 Freiburg, Germany

January 29, 2019

## Abstract

The present study deals with uncertainties in the material response of long fiber reinforced thermoplastics (LFT). In an experimental study, the mechanical response of the material is investigated in direction longitudinal and perpendicular to the fiber preference orientation. Using an optical grey-scale correlation system, local strain measurements on the surface of regular tensile specimens are performed. From the results, local stress-strain curves and material parameters are derived. The results reveal a distinct local variability of the mechanical response of the material due to the variability in the local fiber orientation and fiber density. Based on the experimental observations, a probabilistic elasticity model for LFT materials is proposed. This model allows a numerically efficient virtual prediction of the effect of microstructural disorder of LFT materials on the macroscopic response of structures and structural components.

**Key words:** Long fiber reinforced material, Material model, Microstructural disorder, Uncertainty, Numerical simulation.

## 1 Introduction

Long fiber reinforced thermoplastic (LFT) materials with disordered fiber orientation are important materials in many fields of modern lightweight construction. Being processed by standard processes for polymeric materials such as injection or press molding, long fiber reinforced thermoplastics are especially suitable for industrial scale production (Bijsterbosch and Gaymans [4], Henning et al. [12]). Due to their increased fiber length, typically in the range up to 25, . . . , 50 mm, they feature superior characteristics compared to standard short fiber composites, however, due to the use of well established standard polymer processing methods, they are less expensive than unidirectionally fiber reinforced polymers (Thomason [32]). Furthermore, they can easily be processed to much more complex shapes than unidirectionally fiber reinforced materials. Hence, long fiber reinforced thermoplastic materials are well suited for industrial scale lightweight construction with limited expenses, suitable for all applications, where high, but not extremely high performance materials are required.

One of the major shortcomings of LFT materials is their random disordered microstructure leading to a distinct variability of their macroscopic material properties. Furthermore, since their preferred fiber direction is process dependent, their material properties depend on the flow direction and the completed flow path. Consequently, in a study on the microstructure of injection molded long glass fiber reinforced PA6, Bijsterbosch and Gaymans [4] found a distinct variability in local fiber orientation distribution. For compression molded LFT, based on computed X-ray tomography, Fliegner et al. [8] report similar findings. Considering the effect that in a small control volume different fiber orientations and lengths will be present, a number of LFT material models using ensemble averaging techniques have been proposed in the literature. In this context, Taya and Chou [30] published an analysis of the stress-strain response of short fiber composites based on Eshelby's [7] method, accounting for different fiber orientations based on assumed

---

\*Corresponding author. Tel: +49-761-5142-340, E-mail: joerg.hohe@iwm.fraunhofer.de

†present affiliation: Fraunhofer-Institut für Kurzezeitdynamik Ernst-Mach-Institut EMI, Freiburg, Germany

fiber orientations. A similar analysis, however based on the Mori-Tanaka [21] method and directed to the damage response has been provided by Nguyen and Khaleel [22]. Garesci and Fliegner [10] proposed an analytical model for LFT materials with disordered microstructure, based on the Halpin-Tsai [11] fiber model, forming a simplified form of Hill's [13] self-consistent approach. The LFT model accounts for the fiber orientation distribution, however, the study still provides a deterministic model. In another recent study, Phelps et al. [23] proposed a model for attrition of fibers during the molding process. Here, a distinct variability of the fiber length is found in the final product even for initially constant fiber lengths due to breakages during processing. Other studies on the effective material response of long fiber reinforced thermoplastics with uncertain microstructure using ensemble averaging techniques are due to Dunn et al. [6], Fu and Lauke [9] or Kunc et al. [16]. In a recent contribution, Sharma et al. [26], [27] analyzed the fiber length distribution of carbon fiber based LFT materials using microsectioning in conjunction with optical methods. Based thereon, the elastic constants are determined using the Mori-Tanaka [21] method.

Although they might be based on stochastic considerations regarding the fiber orientations at a specific material point, all LFT material models mentioned above are deterministic material models providing identical material properties for identical input data, i.e. by using ensemble averaging. To deal with the problem of unknown local properties, probabilistic models treat selected or all microstructural parameters as stochastic variables, provided with an appropriate probability distribution. A general review on the uncertainties in fiber reinforced materials resulting from processing such as draping, impregnation or solidification has been provided by Mesogitis et al. [20]. In an experimental approach, Thieme et al. [31] deal with probabilistic effects on the strength of fiber reinforced thermoplastic materials with knitted fiber reinforcement. In a recent contribution, Bednarczyk et al. [3] provided a probabilistic model for infinite fiber reinforced materials dealing with scatter effects caused by uncertain fiber misalignment. A review on application of stochastic approaches to modelling of fiber reinforced composites has been provided by Sriramula and Chryssanthopoulos [29].

Especially in the recent years, a number of contributions with special interest directed to short and long fiber reinforced materials has been provided. Lee and Jasiuk [17] deal with the numerical prediction of the elastic constants for non-infiltrated long fiber networks with disordered microstructure using a probabilistic numerical approach based on a substructure technique. A similar problem is addressed by Dirrenberger et al. [5] using the multiple analysis of testing volume elements with randomly generated microstructure. A numerical prediction of the elastic constants for random short fiber composites has been provided by Lusti et al. [18] using the probabilistic analysis of a multi-fiber representative volume element. Rahman and Chakraborty [24] used the Mori-Tanaka [21] method in conjunction with probabilistic analysis based on the Karhunen-Loève expansion whereas Ma et al. [19] employed the equivalent inclusion method coupled with the random factor method. Altendorf et al. [1] are concerned with modelling of the elastic and thermal response of long fiber reinforced materials using a fast Fourier transform technique considering the uncertain fiber length, orientation, radius and curvature. The assessment of the resulting uncertainties in the effective material response is performed in terms of the basic stochastic moments. Probabilistic methods and models for using the predicted (or experimentally determined) uncertain material data in structural analyses on the macroscopic level have been provided e.g. by Soize [28] or Sakata and Torigoe [25] using a perturbation based approach. The essential base for probabilistic structural analyses using these methods is the availability of a stochastic material model which is able to predict the uncertainty in the effective material properties as well as all correlations between the different properties. In order to be able to provide the information on the correlations in a correct manner, the number of random variables in the model need to be reduced to the essential minimum.

The objective of the present study is an experimental investigation and numerical modelling of uncertainty effects in long fiber reinforced thermoplastic materials deriving from variations in the local fiber orientation and fiber content. In an experimental approach, the scatter in the local (microscopic) strain state in macroscopic specimens under tensile and compressive loads is investigated using a digital image correlation system. The investigation is performed on a glass fiber reinforced polyamide matrix composite as a material example. In a second step, a probabilistic elasticity model is derived. In a similar manner as in a preceding study (Hohe et al. [15]), the model is based on the classical rules of mixture in conjunction with an ensemble averaging technique. In contrast to the earlier model, the local fiber volume fraction and both, the fiber angle within the flow plane of the material and the out-of-plane fiber angle are treated as random variables. The model is validated against the experimental data base. In parametric studies, the effects of the uncertainties in the three-dimensional fiber orientation and the local fiber content on the effective material response are demonstrated.

## 2 Preliminary experimental investigation

### 2.1 Material

As a base for development of the probabilistic elasticity model for long fiber reinforced thermoplastics in Sec. 3, a preliminary experimental investigation has been performed. The objective of this investigation was to study the effects of the microstructural uncertainties on the scatter to be expected in the macroscopic “effective” material properties and to provide a data base for validation of the numerical predictions. The model material system considered is a glass fiber reinforced polyamide 6.6 material (PA66-GF40). With the matrix and fiber densities of  $\rho_{\text{PA66}} = 1.14 \text{ g/cm}^3$  and  $\rho_{\text{GF}} = 2.50 \text{ g/cm}^3$ , the fiber content of 40 wt% coincides with an average fiber volume fraction of  $\rho_f = 23.3\%$ .

The material has been processed by Fraunhofer ICT at Pfinztal in compression molding using the direct LFT (LFT-D) process (Henning et al. [12]). This process consists of a multi-stage procedure. In a first step, the polyamide matrix granulate is compounded in a twin screw extruder. In a second extrusion step, the fibers are added by inserting continuous rovings into a second extruder. The fibers are cut during the second extrusion step in the mixing extruder. As a result, a strand of the raw material is obtained. The LFT-strand is placed into the open mold. By closing the mold, the raw materials is pressed into the cavity to form the final product.

For the present investigation, the material has been provided as plane plate with an average thickness of 2.9 mm. An asymmetric inlay position located at one end of the plate has been used in order to obtain a range with distinct flow path and thus a pronounced fiber re-orientation in the flow range used for the specimen extraction at the opposite end of the plate (see Fig. 1).

### 2.2 Mechanical testing

From the received plates, plane tensile test specimens were machined. The specimen geometry is presented in Fig. 2. Two series of specimens were extracted. For the first series, the test direction coincided with the flow direction (labelled  $0^\circ$ -direction in the following), whereas for the second series ( $90^\circ$ -direction), the specimen axis was oriented perpendicular to the flow direction. The specimens were tested in an Instron 1342 testing machine under displacement control in a quasi-static loading mode till failure. The cross-head velocity was chosen such that an engineering strain rate in the range from  $d\varepsilon_{\text{eng}}/dt = 0.0002 \text{ s}^{-1}$  and  $0.00037 \text{ s}^{-1}$  were obtained. During the tests, the resulting force was continuously recorded using the internal load cell. The local strain measurement was performed by optical means using the ARAMIS grey-scale correlation system. Both, the longitudinal and the transverse strains were determined. The facets for the local strain measurements, their size and position are sketched in Fig. 2. For the basic local assessment, facets with dimensions of  $0.9 \text{ mm} \times 0.9 \text{ mm}$  were used. Since the local uncertainty is related to the size of the evaluation area, additional evaluations of the local strains on larger facets with dimensions of  $1.8 \text{ mm} \times 1.8 \text{ mm}$  and  $3.6 \text{ mm} \times 3.6 \text{ mm}$  were performed by taking the average of  $2 \times 2$  and  $4 \times 4$  arrays of the original  $0.9 \text{ mm} \times 0.9 \text{ mm}$  facets (see Fig. 2). Furthermore, a global engineering strain was determined as the length variation of an initially 10 mm long line in the center of the specimens.

The results for the engineering stress-strain curves on the macroscopic level are presented in Fig. 3(a). As expected, distinct differences between the results for the two testing directions are obtained. For the specimens tested within the flow direction, both, stiffness and strength are approximately 2.5 times higher than for the specimens tested perpendicular to the flow direction. In all cases, the specimens failed in a sudden brittle failure mode without a pronounced preceding ductile damage region. The failure modes are presented in Fig. 3(b). The individual results for the macroscopic elastic moduli  $E_1$  and  $E_2$ , respectively, together with the corresponding ultimate tensile strengths  $R_m$  are compiled in Tab. 1. The results are evaluated in terms of the expectation value  $\mathcal{E}$ , the standard deviation  $S$  and the variability  $S/\mathcal{E}$ . It is observed that both, the elastic moduli  $E_1$  and  $E_2$  within and perpendicular to the fiber direction are subject to distinct variabilities of  $S(E_1)/\mathcal{E}(E_1) = 20.7\%$  and  $S(E_2)/\mathcal{E}(E_2) = 17.8\%$ . With  $S(R_m)/\mathcal{E}(R_m) = 2.9\%$  and  $1.8\%$ , the variabilities for the corresponding strengths are much less pronounced. This result reveals that the material is subject to a distinct scatter especially in its effective stiffness already on the macroscopic level.

### 2.3 Probabilistic evaluation

To investigate the effect of local uncertainties in more detail, a local strain evaluation is performed. As an example, the distribution of the local longitudinal strain  $\varepsilon_{\text{loc}}^{\text{eng}}$  for specimen P3-S-0° is presented in Fig. 4 for five different values of the applied nominal (engineering) strain ( $\varepsilon^{\text{eng}} = 0.5\%, 1\%, 1.5\%, 2\%$  and  $2.5\%$ ) and after specimen failure. At all levels of the applied engineering strain  $\varepsilon^{\text{eng}}$ , a distinct variation of the local engineering strain  $\varepsilon_{\text{loc}}^{\text{eng}}$  is obtained. Even at strain levels well below the failure strain, variabilities in the range of  $\mathcal{S}(\varepsilon_{\text{loc}}^{\text{eng}})/\mathcal{E}(\varepsilon_{\text{loc}}^{\text{eng}}) \approx 10\%$  and beyond are obtained.

For a more detailed investigation of the uncertainty in the local strains  $\varepsilon_{\text{loc}}^{\text{eng}}$ , the local strains  $\varepsilon_{\text{loc}}^{\text{eng}}$  are determined as functions of the nominal macroscopic (engineering) strains  $\varepsilon^{\text{eng}}$ . For a stochastic evaluation, the local results for each individual time increment are re-arranged into ascending order. Assuming a uniform probability for the occurrence of each individual local strain datum  $\varepsilon_{\text{loc}}^{\text{eng}}(t)$ , the (cumulative) probability distributions

$$\mathcal{F}(\varepsilon_{\text{loc}}^{\text{eng}}) = \sum_{i=1}^{j-1} \varepsilon_{\text{loc}(i)}^{\text{eng}} \frac{1}{n} + \varepsilon_{\text{loc}(j)}^{\text{eng}} \frac{1}{2} \frac{1}{n} \quad (1)$$

are obtained, defining the probability that the local strain  $\varepsilon_{\text{loc}}^{\text{eng}}(t)$  has the discrete value  $\varepsilon_{\text{loc}(j)}^{\text{eng}}$  or less. In this context,  $n$  is the total number of local strain data so that

$$p(j) = \frac{1}{n} \quad (2)$$

defines the individual probability for the occurrence of all individual local strain data  $\varepsilon_{\text{loc}(j)}^{\text{eng}}$ .

Care has to be taken in the stochastic evaluation of the experimental results in order to separate aleatoric and epistemic uncertainties, i.e. “true” uncertainties from uncertainties deriving from the employed measurement system. Whereas the former form “physical” uncertainties, really occurring in the physical system under investigation, which cannot be reduced, the latter form uncertainties by inaccuracies in the data acquisition and can be reduced by increasing the accuracy in the data acquisition system. In general, both, the a-priori and the a-posteriori separation of aleatoric and epistemic uncertainties is difficult. In the present study, an a-posteriori approach is used in order to remove the epistemic uncertainties from the data base as far as possible. Considering the entire set of individual local strain vs. local strain curves, a smoothing procedure based on moving averages taken over intervals with increasing width is applied. When taking the moving average over intervals acquired during 6 s, i.e. 11 adjacent data in strain history, a smooth appearance of all local strain vs. local strain curves is obtained which cannot be improved when using larger smoothing intervals. Many of the curves are found to be smooth with no further possible improvements even for smaller smoothing intervals. Nevertheless, in order to ensure that the determined uncertainties are the aleatoric ones caused by the uncertain microstructure of the material, the smoothing interval is fixed to 6 s. All subsequent investigations are based on this interval.

In Fig. 5, the local strains  $\varepsilon_{\text{loc}}^{\text{eng}}$  with cumulative probabilities  $\mathcal{F}(\varepsilon_{\text{loc}}^{\text{eng}}) = 5\%, 25\%, 50\%, 75\%$  and  $95\%$  are plotted against the nominal, macroscopic strain  $\varepsilon^{\text{eng}}$  for the different specimens tested. In this context, the strain data with  $\mathcal{F}(\varepsilon_{\text{loc}}^{\text{eng}}) = 50\%$  define the median value, i.e. the value for  $\varepsilon_{\text{loc}}^{\text{eng}}$ , where 50% of the local strain data are found below and 50% of the strain data are found beyond this value. The curves for the local strain data with  $\mathcal{F}(\varepsilon_{\text{loc}}^{\text{eng}}) = 25\%$  and  $\mathcal{F}(\varepsilon_{\text{loc}}^{\text{eng}}) = 75\%$  as well as  $\mathcal{F}(\varepsilon_{\text{loc}}^{\text{eng}}) = 5\%$  and  $\mathcal{F}(\varepsilon_{\text{loc}}^{\text{eng}}) = 95\%$ , respectively, define envelopes containing the inner 50% and 90% of the local strain data and thus define the scatter band within which the local strain data are expected to be found. The first row of subfigures contains the results for the tensile tests within the flow direction whereas the second row is related to the experiments perpendicular to the flow direction. The results are related to the smallest considered facet size of  $0.9 \text{ mm} \times 0.9 \text{ mm}$ .

In all cases, distinct scatter bands for the local strain levels  $\varepsilon_{\text{loc}}^{\text{eng}}$  are observed. During most of the loading history, the scatter band width in general increases almost linearly with increasing nominal strain level  $\varepsilon^{\text{eng}}$ , indicating a constant variability  $\mathcal{S}(\varepsilon_{\text{loc}}^{\text{eng}})/\mathcal{E}(\varepsilon_{\text{loc}}^{\text{eng}})$  of the results. This approximately constant variability indicates that for the model to be derived in Sec. 3, the use of uncertain elasticity constants with a variability not depending on the actual stress or strain state will be appropriate. In the vicinity of the ultimate failure strain, the local strains tend to localization within the range, where the final failure of the specimen is initiated. The formation of the strain localization results in an increasing scatter band width towards the end of the loading history. The development of a localization zone is more distinct for the experiments perpendicular to the flow direction. For this test direction, the majority of the fibers is

orientated perpendicular to the loading direction. Thus, only a limited number of fibers can form bridges holding the faces of the forming crack together. For the testing direction longitudinal to the flow direction and thus the fiber preference orientation, a higher amount of crack bridges forms prior to final specimen failure. Thus, a more brittle failure mode governed by brittle fiber breakage rather than by more ductile matrix failure is obtained for this test direction.

For an investigation of the effect of the facet size, the probability distributions  $\mathcal{F}(\varepsilon_{loc}^{eng})$  for the local longitudinal strains  $\varepsilon_{loc}^{eng}$  are evaluated for the different facet sizes. The evaluation is performed for nominal strain levels of  $\varepsilon_{loc}^{eng} = 0.5\%$ ,  $1.0\%$ ,  $1.5\%$  and  $2.0\%$  (experiments longitudinal to the flow direction) and  $\varepsilon_{loc}^{eng} = 1.0\%$ ,  $2.0\%$ ,  $3.0\%$  and  $4.0\%$  (experiments perpendicular to the flow direction) as well as at specimen failure. The results are presented in Fig. 6. It is observed that for all cases, the scatter band width, here indicated by the slope of the probability distributions  $\mathcal{F}(\varepsilon_{loc}^{eng})$ , decreases with increasing facet size due to self-averaging effects. This effect occurs in a similar manner for all experiments at all strain levels investigated. Again, a rapidly increasing scatter band width – indicated by a decreasing slope of the probability distributions – is observed, when the ultimate failure strain is approached, especially for the experiments perpendicular to the flow direction. Especially in this range, asymmetric probability distributions of the non-Gaussian type are obtained. Hence, the basic stochastic moments such as the expectation value and the standard deviation alone are insufficient for a comprehensive characterization of the uncertainty effects in the present problem.

The local variations in the microstructure of the material lead to variations in the effective material properties, which subsequently result in the variations in the local strains as investigated in Figs. 4 to 6. To investigate the scatter in the material properties more directly, local elastic constants  $E_i$  and  $\nu_{ij}$  are estimated. For this purpose, local stress-strain curves are approximated from the available data. For the strains, the measured local strain components  $\varepsilon_{ij}^{loc}$  are employed directly, considering both, the  $x_1$ - (flow-) and  $x_2$ - (cross-flow-) directions. The local stresses cannot be measured directly. Therefore, an approximation is necessary. Considering that the local stress state has to satisfy the stress equilibrium, the local variations of the stress components are limited. Since the gauge section of the specimens is of limited size, no excessive stress variations are possible across the gauge section. Therefore, local stresses – in a rough approximation – are assumed to be constant within the gauge section. Thus,  $\sigma_{11}^{loc} \approx \sigma^{eng}$  and  $\sigma_{22}^{loc} \approx 0$  for loading longitudinally to the flow direction whereas  $\sigma_{11}^{loc} \approx 0$  and  $\sigma_{22}^{loc} \approx \sigma^{eng}$  for the experiments perpendicular to the flow direction. In this context,  $\sigma^{eng}$  coincides with the macroscopic engineering strain obtained from the resulting force divided by the specimen section. From the resulting local stress strain curves for the experiments within the flow direction, the local elastic constants

$$E_1^{loc} = \frac{\sigma_{11}^{loc}}{\varepsilon_{11}^{loc}} \quad , \quad \nu_{12}^{loc} = -\frac{\varepsilon_{22}^{loc}}{\varepsilon_{11}^{loc}} \quad (3)$$

are estimated. In a similar manner, the elastic constants

$$E_2^{loc} = \frac{\sigma_{22}^{loc}}{\varepsilon_{22}^{loc}} \quad , \quad \nu_{21}^{loc} = -\frac{\varepsilon_{11}^{loc}}{\varepsilon_{22}^{loc}} \quad (4)$$

are determined from the results based on the experiments perpendicular to the flow direction.

The results for the probability distributions for the estimated local Young's moduli and Poisson's ratios are presented in Figs. 7 and 8, respectively. Again, the probabilistic evaluation is performed for different facet sizes to investigate the self-averaging effect. In addition to the evaluation for the individual specimens (Figs. 7 and 8 (a) to (c)), an evaluation based on the entire data base consisting of the results obtained on all specimens is performed (Figs. 7(d) and 8(d)). Similar as in the probabilistic evaluation of the local strain results, asymmetric, non-Gaussian probability distributions  $\mathcal{F}(E_i)$  are obtained for the estimated local Young's moduli in Fig. 7. The scatter band width decrease with increasing facet size, however, even for the largest facet size of  $3.6 \text{ mm} \times 3.6 \text{ mm}$ , a significant, non-negligible uncertainty in the local Young's moduli for both testing directions is obtained. The short-range uncertainty obtained for the different positions within the gauge sections of the individual specimens is superimposed by a long-range variability between the results obtained on the different specimens. In this context, especially specimen P2-S-0° (see Fig. 7(b)) exhibits a significantly stiffer response compared to the two other specimens tested in the direction longitudinally to the flow direction. In a similar manner, specimen no. P1-S-90° tested perpendicular to the flow direction (see Fig. 7(a)) exhibits an in general lower Young's modulus  $E_2^{loc}$  compared to specimens no. P2-S-90° and P3-S-90°.

For the effective Poisson's ratios  $\nu_{12}^{\text{loc}}$  and  $\nu_{21}^{\text{loc}}$ , an even more distinct uncertainty is observed (see Fig. 8). Due to the fact that the material is anisotropic, the Poisson's ratios are not necessarily restricted to the interval  $\nu_{ij} \in [-0.5, 1]$  as it would be the case for isotropic elasticity. Consequently, a number of data in the upper and lower tail of the probability distributions  $\mathcal{F}(\nu_{ij}^{\text{loc}})$  are found outside the isotropic limits. Again, a distinct self averaging effect resulting in increasingly steep slopes of the probability distributions  $\mathcal{F}(\nu_{ij}^{\text{loc}})$  for increasing facet size is observed. As for the local Young's moduli  $E_i^{\text{loc}}$ , pronounced short-range uncertainties indicated by the widths of the probability distributions  $\mathcal{F}(\nu_{ij}^{\text{loc}})$  for the individual specimens (see Figs. 8(a) to (c)) are superimposed by long-range uncertainties indicated by the different median positions of the probability distributions obtained for the different specimens.

### 3 Probabilistic material model

#### 3.1 Basic assumptions

In order to be able to account for the uncertainties in the material response observed in the experimental investigation, a probabilistic material constitutive model is proposed. The material model is defined in terms of "effective" properties on the macroscopic level of structural hierarchy. All microstructural effects are accounted for in a "smeared" manner in terms of the effects of the essential microstructural parameters on the effective material properties on the macroscopic level. The model is defined in three steps. In a first step, on a strict local level of consideration, the single fiber problem is considered. In a second step, the transition to the multi-fiber problem is made, using the model for the single fiber problem as a basis. In the final step, the obtained, deterministic model is transformed to a probabilistic formulation by treating the uncertain parameters in the formulation as random variables, provided with appropriate probability distributions. This procedure follows the procedure used in a previous study by the authors (Hohe et al. [15]) and generalizes the material model presented there to three-dimensional, uncertain fiber orientations.

In the definition of the probabilistic material model, the number of random variables is kept to its essential minimum in order to account for all correlations between the different stiffness coefficients in the correct manner. By this means, a probabilistic elasticity model is obtained, where the different constants are uncertain, based on the uncertainties in the underlying random variables. In accordance with the observations made in Sec. 2.3 (Fig. 5), no direct effects of the stress or strain state on the uncertainty are assumed.

In order to keep the model as simple as possible, the model is restricted to linear elasticity without consideration of damage or failure. A closed-form formulation is required in order to make the model most suitable for the use on the macroscale in conjunction with e.g. stochastic finite element analyses. For formulation of elasticity models in this sense, two kinds of approaches have been used in literature, i.e. formulations based on the rules of mixture or mean field based approaches using Eshelby's [7] method in conjunction with the Mori-Tanaka [21] approach or self-consistent estimates (Hill [13]). Whereas the latter result in implicit definitions of the constitutive equations, the former two approaches provide closed-form expressions. For the simpler mathematical formulation and for the reason that the approximation of long fibers with aspect ratios in the range of 1:1000 and beyond by ellipsoids seems to be problematic, a formulation based on the rules of mixture is chosen here.

As it is known from literature, the main drivers for the uncertainty in the effective material properties are the fiber density, the fiber orientation and the fiber length. For the latter, Sharma et al. [26], [27] provided an exhaustive experimental evidence. Results of fiber length and orientation distributions have been provided in a previous contribution by Garesci and Fliegner [10] for a material from the identical process, however with a different matrix system using X-ray computed tomography. This study also gives evidence that local variations of the fiber density might be important. On the other hand, e.g. Thomason [32] has shown that the fiber length – provided that it reaches a length as it is typical for LFT materials – is only of minor importance for the stiffness, although strong effects on strength and toughness might still be present. Therefore, the local fiber volume fraction as well as the fiber orientation angles and their probability distributions are assumed as the main drivers for material uncertainty in the present model.

#### 3.2 Formulation

Consider a single fiber according to Fig. 9. The fiber is misaligned with the local flow direction (or any other preference direction) by the angles  $\varphi$  and  $\vartheta$ . For simplicity, a local fiber orientation related Cartesian

coordinate frame  $x'_i$  is introduced, where the  $x'_1$ -direction coincides with the local fiber direction. The overall material response is characterized with respect to the macroscopic Cartesian system  $x_i$  where the  $x_1$ -direction is the flow (or other preference) direction of the composite material. Assuming that the fiber curvature radius and the fiber length are large compared to the fiber diameter and neglecting the possible interaction effects between neighboring fibers, the local elastic properties for the single fiber problem can be estimated by the rules of mixture. Hence, the effective strains and stresses  $\varepsilon'_{ij}$  and  $\sigma'_{ij}$  with respect to the local system  $x'_i$  are interrelated by

$$\begin{pmatrix} \varepsilon'_{11} \\ \varepsilon'_{22} \\ \varepsilon'_{33} \\ 2\varepsilon'_{23} \\ 2\varepsilon'_{13} \\ 2\varepsilon'_{12} \end{pmatrix} = \begin{pmatrix} 1/E'_1 & -\nu'_{21}/E'_2 & -\nu'_{31}/E'_3 & 0 & 0 & 0 \\ & 1/E'_2 & -\nu'_{32}/E'_3 & 0 & 0 & 0 \\ & & 1/E'_3 & 0 & 0 & 0 \\ & & & 1/G'_{23} & 0 & 0 \\ & & & & 1/G'_{13} & 0 \\ \text{(sym.)} & & & & & 1/G'_{12} \end{pmatrix} \begin{pmatrix} \sigma'_{11} \\ \sigma'_{22} \\ \sigma'_{33} \\ \sigma'_{23} \\ \sigma'_{13} \\ \sigma'_{12} \end{pmatrix} \quad (5)$$

with the effective elasticity constants

$$\begin{aligned} E'_1 &= \rho_f E_f + (1 - \rho_f) E_m, & \nu'_{21} &= \frac{E'_2}{E'_1} (\rho_f \nu_f + (1 - \rho_f) \nu_m) \\ E'_2 &= \frac{E_f E_m}{\rho_f E_m + (1 - \rho_f) E_f}, & \nu'_{31} &= \frac{E'_3}{E'_1} (\rho_f \nu_f + (1 - \rho_f) \nu_m) \\ E'_3 &= \frac{E_f E_m}{\rho_f E_m + (1 - \rho_f) E_f}, & \nu'_{32} &= \frac{E'_3}{E'_2} (\rho_f \nu_f + (1 - \rho_f) \nu_m) \\ G'_{23} &= \frac{E'_2}{2(1 + \rho_f \nu_f + (1 - \rho_f) \nu_m)} \\ G'_{13} &= \frac{G_f G_m}{\rho_f G_m + (1 - \rho_f) G_f} \\ G'_{12} &= \frac{G_f G_m}{\rho_f G_m + (1 - \rho_f) G_f} \end{aligned} \quad (6)$$

where  $E_f$ ,  $G_f$  and  $\nu_f$  as well as  $E_m$ ,  $G_m$  and  $\nu_m$  are the elastic constants for the fiber and matrix material respectively whereas  $\rho_f$  denotes the fiber volume fraction. By inversion of Eq. (5),

$$\begin{pmatrix} \sigma'_{11} \\ \sigma'_{22} \\ \sigma'_{33} \\ \sigma'_{23} \\ \sigma'_{13} \\ \sigma'_{12} \end{pmatrix} = \begin{pmatrix} C'_{1111} & C'_{1122} & C'_{1133} & C'_{1123} & C'_{1113} & C'_{1112} \\ & C'_{2222} & C'_{2233} & C'_{2223} & C'_{2213} & C'_{2212} \\ & & C'_{3333} & C'_{3323} & C'_{3313} & C'_{3312} \\ & & & C'_{2323} & C'_{2313} & C'_{2312} \\ & & & & C'_{1313} & C'_{1312} \\ \text{(sym.)} & & & & & C'_{1212} \end{pmatrix} \begin{pmatrix} \varepsilon'_{11} \\ \varepsilon'_{22} \\ \varepsilon'_{33} \\ 2\varepsilon'_{23} \\ 2\varepsilon'_{13} \\ 2\varepsilon'_{12} \end{pmatrix} \quad (7)$$

the components  $C'_{ijkl}$  of the fourth order elasticity tensor in the tensorial form

$$\sigma'_{ij} = C'_{ijkl} \varepsilon'_{kl} \quad (8)$$

of Hooke's law for the single fiber problem are obtained with respect to the local coordinate system  $x'_i$ . The elasticity tensor  $C'_{ijkl}$  is transformed from the local coordinate system  $x'_i$  into the global system  $x_j$  by means of the standard transformation

$$C_{ijkl} = a_{im} a_{jn} a_{kp} a_{lq} C'_{mnpq} \quad (9)$$

with the transformation matrix

$$a_{ij} = \begin{pmatrix} \cos \varphi \cos \vartheta & -\sin \varphi & \cos \varphi \sin \vartheta \\ \sin \varphi \cos \vartheta & \cos \varphi & \sin \varphi \sin \vartheta \\ -\sin \vartheta & 0 & \cos \vartheta \end{pmatrix} \quad (10)$$

where  $\varphi$  and  $\vartheta$  are the local fiber orientation angles according to Fig. 9. As a result, the components  $C_{ijkl}$  of the effective stiffness tensor for the single fiber problem are available.

In the second step, the effective stiffness components  $\bar{C}_{ijkl}$  for the multi-fiber problem are to be determined. The effective stiffness components  $\bar{C}_{ijkl}$  are derived from the corresponding single-fiber coefficients  $C_{ijkl}$  by a stochastic consideration: As sketched in Fig. 9, a statistically representative volume element for

the multi-fiber material consists of a large number of smaller single-fiber volume elements as considered in Eqns. (5) to (10). The orientations of the single fibers are random, described in terms of the probability density distributions  $f_\varphi(\varphi)$  and  $f_\vartheta(\vartheta)$  for the fiber angles  $\varphi$  and  $\vartheta$ . The probability density distributions can be of any feasible type.

Assuming that the fiber angles are uncorrelated, i.e. their probability distributions are independent from each other, a separation ansatz of the type

$$f_{\varphi\vartheta}(\varphi, \vartheta) = f_\varphi(\varphi) f_\vartheta(\vartheta) \quad (11)$$

is employed so that the total probability density for the two variable  $\varphi$  and  $\vartheta$  is defined as the product of the two one-dimensional probability density distributions  $f_\varphi(\varphi)$  and  $f_\vartheta(\vartheta)$ . For the fiber angle  $\varphi$  within the  $x_1$ - $x_2$ -plane, i.e. the tangential plane of a thin-walled long fiber reinforced thermoplastic structure, a truncated Gaussian probability density distribution

$$f_\varphi(\varphi) = \begin{cases} \frac{1}{c_\varphi} \frac{1}{s_\varphi(2\pi)^{1/2}} e^{-\frac{1}{2} \frac{(\mu_\varphi - \varphi)^2}{s_\varphi^2}} & \text{for: } -\frac{\pi}{2} < \varphi \leq \frac{\pi}{2} \\ 0 & \text{elsewhere} \end{cases} \quad (12)$$

is assumed, where  $\mu_\varphi$  and  $s_\varphi$  are material parameter, describing the preferred fiber orientation and the scatter band width, respectively. The truncation to the interval  $\varphi \in [-\pi/2, \pi/2]$  is necessary, since due to the  $\pi$ -periodicity, a rotation of an individual fiber by an angle of  $\varphi = n\pi$  or  $\vartheta = n\pi$  results in the initial orientation. Hence, the fiber angle definitions are only feasible in the interval  $\varphi, \vartheta \in [-\pi/2, \pi/2]$ . For all rotations outside this interval, a corresponding problem inside the interval can be defined. The parameter  $c_\varphi$  has to be chosen such that

$$\int_{-\frac{\pi}{2}}^{\frac{\pi}{2}} f_\varphi(\varphi) d\varphi = 1 \quad (13)$$

holds for the respective values of the material properties  $\mu_\varphi$  and  $s_\varphi$ . The probability density distribution for the second fiber angle  $\vartheta$ , a similar truncated Gaussian distribution

$$f_\vartheta(\vartheta) = \begin{cases} \frac{1}{c_\vartheta} \frac{\cos \vartheta}{s_\vartheta(2\pi)^{1/2}} e^{-\frac{1}{2} \frac{(\mu_\vartheta - \vartheta)^2}{s_\vartheta^2}} & \text{for: } -\frac{\pi}{2} < \vartheta \leq \frac{\pi}{2} \\ 0 & \text{elsewhere} \end{cases} \quad (14)$$

which in addition is warped by the factor  $\cos \vartheta$  in order to ensure that a uniform probability density over the considered semi-sphere of the possible fiber angles is obtained, if both,  $s_\varphi \rightarrow \infty$  and  $s_\vartheta \rightarrow \infty$ . Again,  $\mu_\vartheta$  and  $s_\vartheta$  form material parameters, whereas the parameter  $c_\vartheta$  is chosen such that

$$\int_{-\frac{\pi}{2}}^{\frac{\pi}{2}} f_\vartheta(\vartheta) d\vartheta = 1 \quad (15)$$

holds in order to correct the errors due to the truncation and warping of the Gaussian distribution. If the mean fiber orientation coincides with the flow direction according to Fig. 9,  $\mu_\varphi = \mu_\vartheta = 0$  so that the two scatter parameters  $s_\varphi$  and  $s_\vartheta$  are the only remaining additional parameters. In the case of a non-truncated, non-warped definition of the probability density distributions (12) and (14), i.e. in the case that the probability density distributions were of the true Gaussian type, the parameters  $s_\varphi$  and  $s_\vartheta$  would define the standard deviations of the individual probability density distributions for the fiber angles.

Considering the probability density distributions  $f_\varphi(\varphi)$  and  $f_\vartheta(\vartheta)$  for the fiber angles  $\varphi$  and  $\vartheta$ , the effective material properties for the ensemble of the multi-fiber material can be defined as the expectation value

$$\bar{C}_{ijkl} = \mathcal{E}(C_{ijkl}) = \int_{\vartheta=-\infty}^{\infty} \int_{\varphi=-\infty}^{\infty} C_{ijkl}(\varphi, \vartheta) f_\varphi(\varphi) f_\vartheta(\vartheta) d\varphi d\vartheta \quad (16)$$

of the local material stiffness components  $C_{ijkl}$  defined by Eqns. (8) and (9) for the single fiber problem. Through Eqns. (5) to (14), Eq. (16) defines the effective stiffness tensor  $\bar{C}_{ijkl}$  for the long fiber reinforce

thermoplastic as a function of the elastic constants  $E_f$ ,  $\nu_f$ ,  $E_m$  and  $\nu_m$  of the fibers and the matrix, respectively, as well as the local fiber volume fraction  $\rho_f$  and the parameters  $s_\varphi$  and  $s_\vartheta$  defining the scatter band widths of the fiber orientation distributions around the  $x_1$ -direction as the preferred fiber direction. If the preferred direction (flow direction) does not coincide with the  $x_1$ -direction, the two additional variables  $\mu_\varphi$  and  $\mu_\vartheta$  enter as additional parameters defining the preferred direction.

### 3.3 Probabilistic enhancement

The material constitutive model (5) to (16), although relying on a stochastic consideration in terms of the ensemble average (16), still provides a deterministic constitutive description of the material behavior, as long as all microstructure related input variables  $E_f$ ,  $\nu_f$ ,  $E_m$ ,  $\nu_m$ ,  $\rho_f$ ,  $\mu_\varphi$ ,  $s_\varphi$ ,  $\mu_\vartheta$  and  $s_\vartheta$  are provided with deterministically exact values. Nevertheless, especially the essential microstructure related parameters, i.e. the local fiber volume fraction  $\rho_f$  as well as the position and scatter parameters  $\mu_\varphi$ ,  $s_\varphi$ ,  $\mu_\vartheta$  and  $s_\vartheta$  for the local fiber probability density distributions are subject to local uncertain variations.

In an probabilistic enhancement of the multi-fiber material model (16), the local relative density  $\rho_f$  as well as the parameters  $s_\varphi$  and  $s_\vartheta$  are treated as random variables. In a simplifying approach, the parameters  $\mu_\varphi$  and  $\mu_\vartheta$  defining the fiber preference direction are treated as zero, assuming that the preference orientation coincides with the  $x_1$ -direction. The random variables are provided with appropriate probability distributions, describing the probability for the occurrence of specific values for the respective variables. In the present study, the distribution of the random variables are approximated by logarithmic normal distributions

$$f(\rho_f) = \frac{1}{\rho_f S_\rho (2\pi)^{1/2}} e^{-\left(\frac{\ln \rho_f - M_\rho}{2^{1/2} S_\rho}\right)^2} \quad (17)$$

$$f(s_\varphi) = \frac{1}{s_\varphi S_\varphi (2\pi)^{1/2}} e^{-\left(\frac{\ln s_\varphi - M_\varphi}{2^{1/2} S_\varphi}\right)^2} \quad (18)$$

$$f(s_\vartheta) = \frac{1}{s_\vartheta S_\vartheta (2\pi)^{1/2}} e^{-\left(\frac{\ln s_\vartheta - M_\vartheta}{2^{1/2} S_\vartheta}\right)^2} \quad (19)$$

in order to avoid the problem of the occurrence of negative values for the fiber volume fraction  $\rho_f$  as well as the scatter band parameters  $s_\varphi$  and  $s_\vartheta$ . The parameters of the logarithmic normal distributions (17) to (19) are defined by

$$M_\rho = \ln(\mathcal{E}(\rho_f)) - \frac{1}{2} \ln\left(\left(\frac{\mathcal{S}(\rho_f)}{\mathcal{E}(\rho_f)}\right)^2 + 1\right), \quad S_\rho = \left(\ln\left(\left(\frac{\mathcal{S}(\rho_f)}{\mathcal{E}(\rho_f)}\right)^2 + 1\right)\right)^{\frac{1}{2}} \quad (20)$$

$$M_\varphi = \ln(\mathcal{E}(s_\varphi)) - \frac{1}{2} \ln\left(\left(\frac{\mathcal{S}(s_\varphi)}{\mathcal{E}(s_\varphi)}\right)^2 + 1\right), \quad S_\varphi = \left(\ln\left(\left(\frac{\mathcal{S}(s_\varphi)}{\mathcal{E}(s_\varphi)}\right)^2 + 1\right)\right)^{\frac{1}{2}} \quad (21)$$

$$M_\vartheta = \ln(\mathcal{E}(s_\vartheta)) - \frac{1}{2} \ln\left(\left(\frac{\mathcal{S}(s_\vartheta)}{\mathcal{E}(s_\vartheta)}\right)^2 + 1\right), \quad S_\vartheta = \left(\ln\left(\left(\frac{\mathcal{S}(s_\vartheta)}{\mathcal{E}(s_\vartheta)}\right)^2 + 1\right)\right)^{\frac{1}{2}} \quad (22)$$

in terms of the expectation values  $\mathcal{E}(\rho_f)$ ,  $\mathcal{E}(s_\varphi)$  and  $\mathcal{E}(s_\vartheta)$  of the random variables  $\rho_f$ ,  $s_\varphi$  and  $s_\vartheta$  as well as their standard deviations  $\mathcal{S}(\rho_f)$ ,  $\mathcal{S}(s_\varphi)$  and  $\mathcal{S}(s_\vartheta)$ , respectively.

The parameters controlling the probability distributions for the microstructural random variables can easily be determined experimentally during the microstructural characterization of the material using computed tomography or other suitable methods.

### 3.4 Numerical implementation

The evaluation of the probability distributions  $\mathcal{F}(\bar{C}_{ijkl})$  for the effective stiffness coefficients of the material according to Eq. (16) in dependence on the (known) probability distributions of the stochastic variables  $\rho_f$ ,  $s_\varphi$  and  $s_\vartheta$  according to Eqns. (17) to (19) is performed numerically. For the stochastic analysis, different

numerical schemes have been proposed in the literature. The simplest among these methods is the direct Monte-Carlo scheme, where a large set of discrete, randomly determined combinations need to be analyzed. In order to avoid the extreme numerical effort required for a Monte-Carlo simulation, a discretizing numerical scheme, established in a previous contribution (Beckmann and Hohe [2]), is employed in the present study in order to keep the numerical effort within acceptable bounds.

This scheme is based on a predefined discretization of the (hyper-) space of the random variables, as sketched in Fig. 10. For each of the random variables, a number of discrete values  $\rho_f^{(p)}$ ,  $s_\varphi^{(q)}$  and  $s_\vartheta^{(r)}$  with  $p = 1, \dots, p_{\max}$ ,  $q = 1, \dots, q_{\max}$  and  $r = 1, \dots, r_{\max}$  is considered. Each of the discrete values of the random variables is provided with an interval  $\Delta\rho_f^{(p)}$ ,  $\Delta s_\varphi^{(q)}$  and  $\Delta s_\vartheta^{(r)}$ , i.e. the interval ranging from the mid-points between the respective discrete value of the respective random variable and its nearest neighbors (see Fig. 10). Considering the probability density distributions (17) to (19) for the random variables, the individual probability  $\Delta\mathcal{F}$  of occurrence for each discrete value of the random variables is obtained by the integration

$$\Delta\mathcal{F}(\rho_f^{(p)}) = \int_{\rho_f^{(p)} - \frac{1}{2}\Delta\rho_f^{(p)}}^{\rho_f^{(p)} + \frac{1}{2}\Delta\rho_f^{(p)}} f_{\ln}(\rho_f) d\rho_f \quad (23)$$

$$\Delta\mathcal{F}(s_\varphi^{(q)}) = \int_{s_\varphi^{(q)} - \frac{1}{2}\Delta s_\varphi^{(q)}}^{s_\varphi^{(q)} + \frac{1}{2}\Delta s_\varphi^{(q)}} f_{\ln}(s_\varphi) ds_\varphi \quad (24)$$

$$\Delta\mathcal{F}(s_\vartheta^{(r)}) = \int_{s_\vartheta^{(r)} - \frac{1}{2}\Delta s_\vartheta^{(r)}}^{s_\vartheta^{(r)} + \frac{1}{2}\Delta s_\vartheta^{(r)}} f_{\ln}(s_\vartheta) ds_\vartheta \quad (25)$$

of the probability density distributions with respect to the intervals assigned to the respective discrete values of the random variables. Since the random variables in the present problem are entirely uncorrelated, the individual probability for occurrence of the combination of the discrete values  $\rho_f^{(p)}$ ,  $s_\varphi^{(q)}$  and  $s_\vartheta^{(r)}$  is defined by the product

$$\Delta\mathcal{F}(\rho_f^{(p)}, s_\varphi^{(q)}, s_\vartheta^{(r)}) = \Delta\mathcal{F}(\rho_f^{(p)}) \Delta\mathcal{F}(s_\varphi^{(q)}) \Delta\mathcal{F}(s_\vartheta^{(r)}) \quad (26)$$

of the probabilities for occurrence of the respective values for the individual random variables.

Eq. (26) with Eqns. (23) to (25) defines the probability for occurrence of the set  $(\rho_f^{(p)}, s_\varphi^{(q)}, s_\vartheta^{(r)})$  of discrete values for the random variables and thus also defines the probability

$$\Delta\mathcal{F}(\bar{C}_{ijkl}^{(pqr)}) = \Delta\mathcal{F}(\bar{C}_{ijkl}(\rho_f^{(p)}, s_\varphi^{(q)}, s_\vartheta^{(r)})) = \Delta\mathcal{F}(\rho_f^{(p)}, s_\varphi^{(q)}, s_\vartheta^{(r)}) \quad (27)$$

for each homogenization result based thereon. Hence, the probability distributions  $\mathcal{F}(\bar{C}_{ijkl})$  for the effective stiffness components  $\bar{C}_{ijkl}$  are easily obtained by computing the effective stiffness components for each “node”  $(\rho_f^{(p)}, s_\varphi^{(q)}, s_\vartheta^{(r)})$  in the discretizes space of the random variables, re-arranging the results into ascending order and providing each of the data with its individual probability increment  $\Delta\mathcal{F}(\bar{C}_{ijkl}^{(pqr)})$ . Subsequently, the cumulative probability for the  $s$ -th homogenization result is given by

$$\mathcal{F}(\bar{C}_{ijkl}^{(s)}) = \sum_{t=1}^{s-1} \Delta\mathcal{F}(\bar{C}_{ijkl}^{(t)}) + \frac{1}{2} \Delta\mathcal{F}(\bar{C}_{ijkl}^{(s)}) \quad (28)$$

with

$$\bar{C}_{ijkl}^{(t)} \geq \bar{C}_{ijkl}^{(t-1)} \quad \text{for: } t = 2, \dots, p_{\max}q_{\max}r_{\max} \quad (29)$$

(see Fig. 10). The advantage of this discretization strategy compared to direct Monte-Carlo simulation and also more advanced techniques as e.g. latin hyper-cube methods, which involve a random determination of the discrete “nodes”  $(\rho_f^{(p)}, s_\varphi^{(q)}, s_\vartheta^{(r)})$  for evaluation of the kernel is that the location of the “nodes” in the space of the random variables is pre-defined. Hence, areas of special interest or strong variations of the kernel can easily be provided with a denser “mesh” in order to improve the accuracy of the solution, resulting in a numerically more efficient analysis.

## 4 Results

### 4.1 Material data

The probabilistic material model developed in Sec. 3 is now applied to the PA66-GF40 long fiber reinforced thermoplastic material described in Sec. 2.1. According to the nominal fiber mass content of 40%, an expectation value of  $\mathcal{E}(\rho_f) = 0.233$  is considered for the fiber volume fraction  $\rho_f$ . Since the fiber volume fraction for LFT materials is subject to spatial variations, a standard deviation of  $\mathcal{S}(\rho_f) = 0.05$  is assumed. For the scatter band parameters for the fiber orientation angles of the tested material, no direct experimental data is available. Nevertheless, from tomographic investigations on similar long fiber reinforced thermoplastic materials (Fliegner et al. [8]), the assumptions of  $\mathcal{E}(s_\varphi) = 0.25\pi$  and  $\mathcal{S}(s_\varphi) = 0.05\pi$  for the expectation value and the standard deviation of the scatter band parameter  $s_\varphi$  of the in-plane fiber angle in the flow range appear to be a suitable assumption. The transverse fiber angle  $\vartheta$  (see Fig. 9) is bounded more strictly due to geometric restrictions by the fiber length exceeding the wall thickness of typical thin-walled LFT structures. Hence,  $\mathcal{E}(s_\vartheta) = 0.1\pi$  and  $\mathcal{S}(s_\vartheta) = 0.02\pi$  are assumed for the transverse scatter band parameter  $s_\vartheta$  of the fiber orientation through the plate thickness. These values for the expectation value and standard deviation of the stochastic variables  $\rho_f$ ,  $s_\varphi$  and  $s_\vartheta$  are considered as the base state for the parametric studies presented in the following sections.

For the glass fibers, a Young's modulus of  $E_f = 73$  GPa and a Poisson's ratio of  $\nu_f = 0.23$  are common choices. Assuming that the material has been subjected to ambient moisture for a while as it has been the case in the experiments, a Young's modulus of  $E_m = 1.5$  GPa and thus towards the lower end of the range for polyamide 6.6 is considered for the matrix. The Poisson's ratio of the matrix is set to  $\nu_m = 0.39$  providing a typical value for PA66.

In the numerical simulation, the space of the random variables is discretized into equidistant intervals (see Fig. 10). For the fiber volume fraction, 30 intervals with an element length of  $\Delta\rho_f = 0.02$  covering the interval  $\rho_f \in [0.03, 0.43]$  are employed. The fiber orientation scatter band parameters  $s_\varphi$  and  $s_\vartheta$  are discretized into 19 elements each. The element widths are set to  $\Delta s_\varphi = 0.025\pi$  and  $\Delta s_\vartheta = 0.01\pi$ , covering the ranges  $s_\varphi \in [0.025\pi, 0.5\pi]$  and  $s_\vartheta \in [0.01\pi, 0.2\pi]$ , respectively.

### 4.2 Effect of uncertainties in the fiber volume fraction

In a first parametric study, the effect of uncertainties in the fiber volume fraction  $\rho_f$  is studied. The results are presented in Fig. 11. In this figure, as well as in all subsequent figures providing the results of the parametric studies regarding the effect of the expectation values and the standard deviations of the stochastic variables, the first row of subfigures (Figs. 11(a), (c) and (e)) is related to variations in the expectation value of the stochastic variable considered whereas the second row of subfigures (Figs. 11(b), (d) and (f)) is related to the effect of its standard deviation as indicated in the legend. The expectation values and standard deviations of all stochastic variables not mentioned in the legends are kept at their base values as mentioned in Sec. 4.1. The first line of subfigures (Figs. 11(a) and (b)) provides the probability distributions  $\mathcal{F}(\bar{E}_i)$  of the effective Young's moduli  $\bar{E}_i$ . The second line of subfigures (Figs. 11(c) and (d)) provides the probability distributions  $\mathcal{F}(\bar{G}_{ij})$  for the effective shear moduli  $\bar{G}_{ij}$ , whereas the probability distributions  $\mathcal{F}(\bar{\nu}_{ij})$  for the effective Poisson's ratios  $\bar{\nu}_{ij}$  are presented in the last line of subfigures (Figs. 11(e) and (f)). In all cases, no smoothing has been applied to the numerical results. Hence, a "staircase"-type characteristic of the probability distributions is observed in those cases, where the discretization of the space of the stochastic variables is too coarse for a smooth transition between the probabilities for the individual data, e.g. towards the lower tail of the probability distribution  $\mathcal{F}(\bar{G}_{12})$  for the effective shear modulus  $\bar{G}_{12}$  for the case  $\mathcal{E}(\rho_f) = 0.133$  (see Fig. 11(c)). Due to the rough estimates obtained for the integrals of the probability density functions for the stochastic variables in these cases by the numerical integration scheme, the resulting probability functions do not approach the limit of  $\mathcal{F} = 1$  in their upper tails in an absolutely precise manner. In order to avoid confusion, this (small, but in some cases not vanishingly small) numerical integration inaccuracy has been corrected by a correcting scaling of the distributions.

In all cases considered in Fig. 11, a distinct uncertainty in the effective material properties is observed. For the different effective material properties, different effects of uncertainties in the underlying stochastic variables are obtained, i.e. wide scatter bands are obtained for the in-plane elastic moduli  $\bar{E}_1$  and  $\bar{E}_2$  whereas for the transverse elastic modulus  $\bar{E}_3$  a rather steep increase of the probability distribution  $\mathcal{F}(\bar{E}_3)$  is obtained, indicating a low sensitivity to variations in the fiber volume fraction  $\rho_f$  (see Fig. 11(a)). A variation in the expectation value  $\mathcal{E}(\rho_f)$  of the fiber volume fraction  $\rho_f$  results in a shift of the probability

density distributions  $\mathcal{F}(\bar{E}_i)$  with respect to their arguments  $\bar{E}_i$ . The most distinct effect is obtained for the in-plane Young's modulus  $\bar{E}_1$  within the fiber orientation preference direction, whereas less pronounced but still distinct effects occur for the in-plane Young's modulus  $\bar{E}_2$  perpendicular to the fiber preference direction. The probability distribution for the transverse Young's modulus  $\bar{E}_3$  exhibits only a minor dependence on variations in the expectation value  $\mathcal{E}(\rho_f)$  of the fiber volume fraction (see Fig. 11(a)). As it can be observed in Fig. 11(b), variation of the standard deviation  $\mathcal{S}(\rho_f)$  of the fiber volume fraction results in an increase or decrease of the scatter band width, indicated by the slope of the probability distributions  $\mathcal{F}(\bar{E}_i)$  of the effective elastic moduli  $\bar{E}_i$ . Again, the most distinct effects are obtained for the in-plane Young's modulus  $\bar{E}_1$  within the fiber preference direction, followed by the second in-plane Young's modulus  $\bar{E}_2$  perpendicular to this direction, whereas the transverse Young's modulus  $\bar{E}_3$  remains almost unaffected.

The strong sensitivity of the probability distribution  $\mathcal{F}(\bar{E}_1)$  of the in-plane Young's modulus  $\bar{E}_1$  within the fiber preference direction and the less pronounced sensitivities of the probability distributions for the second in-plane Young's modulus  $\bar{E}_2$  and especially the transverse Young's modulus  $\bar{E}_3$  are caused by the amount of fibers oriented towards the respective directions. Since the elastic moduli longitudinal and perpendicular to the fiber direction in the single fiber problem are assumed to be governed by the linear and reciprocal rules of mixture (6), the effective elastic modulus longitudinal to the fiber direction of the single fiber problem depends in a linear manner on the fiber volume fraction  $\rho_f$  throughout its entire possible range. According to the reciprocal rule of mixture, the effective elastic moduli transversal to the fiber direction exhibit an only weak dependence on the fiber volume fraction  $\rho_f$  in the range of low  $\rho_f$ . Thus, for the single fiber problem, the sensitivity of the elastic moduli on the fiber volume fraction is more pronounced for the longitudinal Young's modulus than for the Young's moduli perpendicular to the fiber direction. Hence, strong effects of the fiber volume fraction  $\rho_f$  are obtained in the multi fiber problem – which is derived by ensemble averaging of the single fiber solution – for all cases, where a large amount of fibers is oriented towards the respective direction, i.e. especially the preference direction for the fiber orientation ( $x_1$ -direction).

For the probability distributions  $\mathcal{F}(\bar{G}_{ij})$  for the effective shear moduli  $\bar{G}_{ij}$  presented in Figs. 11(c) and (d), strong effects of variations in the expectation value  $\mathcal{E}(\rho_f)$  and the standard deviation  $\mathcal{S}(\rho_f)$  of the fiber volume fraction  $\rho_f$  are obtained especially in case of the in-plane shear modulus  $\bar{G}_{12}$ . The effects on the probability distributions for the two transverse shear moduli  $\bar{G}_{23}$  and  $\bar{G}_{13}$  are less pronounced. Again, this effect is caused by the larger amount of fibers oriented in different directions within the  $x_1$ - $x_2$ -plane. Through the ensemble averaging procedure, these fibers contribute significantly to the in-plane shear modulus. As a consequence, (i) rather high in-plane shear moduli  $\bar{G}_{12}$  are obtained, which are (ii) highly sensitive with respect to variations in both, the expectation value  $\mathcal{E}(\rho_f)$  of the fiber volume fraction  $\rho_f$  (Fig. 11(c)) and its standard deviation  $\mathcal{S}(\rho_f)$  (Fig. 11(d)). For the transverse shear moduli, which are matrix-controlled, lower and less sensitive values are obtained. In this context, the shear modulus  $\bar{G}_{13}$  within the  $x_1$ - $x_3$ -plane, involving the fiber preference ( $x_1$ -) direction exhibits slightly higher values and a slightly more pronounced sensitivity on the fiber volume fraction  $\rho_f$  than the second transverse shear modulus  $\bar{G}_{23}$ . Again, variations of the expectation value  $\mathcal{E}(\rho_f)$  of the fiber volume fraction  $\rho_f$  result in a shift of the probability distributions  $\mathcal{F}(\bar{G}_{ij})$  with respect to their arguments whereas variations in the standard deviation  $\mathcal{S}(\rho_f)$  affect predominantly the scatter band widths of the results, indicated by the slope of the probability distributions  $\mathcal{F}(\bar{G}_{ij})$  for the effective shear moduli  $\bar{G}_{ij}$ .

For the probability distributions  $\mathcal{F}(\bar{\nu}_{ij})$  of the effective Poisson's ratios  $\bar{\nu}_{32}$ ,  $\bar{\nu}_{31}$  and  $\bar{\nu}_{21}$ , presented in Figs. 11(e) and (f), effects of the fiber volume fraction  $\rho_f$  enter predominantly through its expectation value  $\mathcal{E}(\rho_f)$  (Fig. 11(e)), whereas they are found insensitive with regard to variation in its standard deviation  $\mathcal{S}(\rho_f)$  (Fig. 11(f)).

A comparison of the results for the probability distributions  $\mathcal{F}(\bar{E}_i)$  for the two in-plane Young's moduli  $\bar{E}_1$  and  $\bar{E}_2$  within and perpendicular to the fiber preference ( $x_1$ -) direction in Figs. 11(a) and (b) for the reference case (i.e.  $\mathcal{E}(\rho_f) = 0.233$ ) with experimental data in Fig. 7 yields a rather good agreement, concerning both, the median values and the slopes of the probability distributions. Especially with the experimental results obtained on specimens no. P3-S-0° and P3-S-90° (Fig. 7(c)), an excellent agreement is observed. For the probability distributions  $\mathcal{F}(\bar{\nu}_{21})$  of the in-plane Poisson's ratio  $\bar{\nu}_{21}$ , the position of the scatter band in terms of the median of the probability distribution is predicted with a good accuracy (see Figs. 8 and 11(f)). The scatter band width observed in the experimental investigation is underestimated by the model. On the other hand, it has to be considered that an accurate measurement of the strains perpendicular to the loading direction is rather difficult, especially for small strains  $\varepsilon_{22}$ . Hence, the lower tails of the probability distributions  $\mathcal{F}(\bar{\nu}_{ij})$  in Fig. 8 might be subject to measurement inaccuracies (or epistemic uncertainties)

when the experimentally determined Poisson's ratio approaches zero. Nevertheless, regarding the experimentally determined probability distributions based on the facets with edge lengths of  $3.6 \text{ mm} \times 3.6 \text{ mm}$ , even here, a reasonable agreement between experimental data and numerical prediction is obtained.

### 4.3 Effect of uncertainties in the fiber orientation

Further to the fiber volume fraction, the in-plane and transverse fiber orientation scatter band parameters  $s_\varphi$  and  $s_\vartheta$  are treated as random variables. The effects of their expectation values  $\mathcal{E}(s_\varphi)$  and  $\mathcal{E}(s_\vartheta)$  as well as their standard deviations  $\mathcal{S}(s_\varphi)$  and  $\mathcal{S}(s_\vartheta)$  are investigated in Figs. 12 and 13 respectively. All expectation values and standard deviations of the three random variables not mentioned in the figure legends are kept constant at their base values as mentioned in Sec. 4.1. The subfigures in Figs. 12 and 13 are arranged in the same manner as in Fig. 11 (see Sec. 4.2).

For the in-plane fiber orientation scatter band parameter  $s_\varphi$  investigated in Fig. 12, strong effects of changes in its expectation value  $\mathcal{E}(s_\varphi)$  are observed with respect to the in-plane elastic moduli (effective Young's moduli  $\bar{E}_1$  and  $\bar{E}_2$  as well as effective shear modulus  $\bar{G}_{12}$  presented in Figs. 12(a) and (c)), especially when the expectation value  $\mathcal{E}(s_\varphi)$  approaches small values, i.e. when the case of a nearly uniaxially reinforced microstructure is approached. In this case, the probability distributions  $\mathcal{F}(\bar{E}_1)$  and  $\mathcal{F}(\bar{E}_2)$  feature an increasing distance to each other, where  $\mathcal{F}(\bar{E}_1)$  is shifted towards larger  $\bar{E}_1$  whereas  $\mathcal{F}(\bar{E}_2)$  is shifted towards lower effective Young's moduli. For the probability distribution  $\mathcal{F}(\bar{G}_{12})$  for the effective in-plane shear modulus  $\bar{G}_{12}$ , a distinct shift towards low shear moduli is observed when the microstructure approaches the unidirectionally reinforced type at  $s_\varphi \rightarrow 0$ . In this case, the effective shear modulus approaches the limit of the matrix shear modulus. In this context, the corresponding probability distribution is not only shifted towards low  $\bar{G}_{12}$  but also changes its shape towards an asymmetric, essentially non-Gaussian type (see Fig. 12(c)).

Towards the upper end of the considered interval of  $\mathcal{E}(s_\varphi)$ , the microstructure approaches an entirely disordered type, such as it will develop i.e. in the strand inlay ranges. In this case, the probability distributions  $\mathcal{F}(\bar{E}_1)$  and  $\mathcal{F}(\bar{E}_2)$  for the two in-plane Young's moduli  $\bar{E}_1$  and  $\bar{E}_2$  approach each other (see Fig. 12(a)). The in-plane shear modulus  $\bar{G}_{12}$  approaches much larger values than in the unidirectionally reinforced limit, due to the increasing amount of fibers oriented in different directions. For the probability distributions  $\bar{\nu}_{ij}$  of the effective Poisson's ratios  $\bar{\nu}_{ij}$ , distinct effects of variations in the expectation value  $\mathcal{E}(s_\varphi)$  of the fiber orientation scatter band parameter are observed especially for the two Poisson's ratios  $\bar{\nu}_{32}$  and  $\bar{\nu}_{21}$ . Again, asymmetric, essentially non-Gaussian probability distributions are observed in the low fiber orientation variability limit.

The effect of variations in the standard deviation  $\mathcal{S}(s_\varphi)$  of the in-plane scatter band parameter  $s_\varphi$  is investigated in Figs. 12(b), (d) and (f). Compared to variations in its expectation value  $\mathcal{E}(s_\varphi)$  (Figs. 12(a), (c) and (e)), less distinct effects are observed. The only exceptions are the lower tail of the probability distribution  $\mathcal{F}(\bar{E}_2)$  for the in-plane Young's modulus  $\bar{E}_2$  perpendicular to the fiber preference direction as well as the probability distributions  $\mathcal{F}(\bar{\nu}_{32})$  and  $\mathcal{F}(\bar{\nu}_{21})$  for the effective Poisson's ratios  $\bar{\nu}_{32}$  and  $\bar{\nu}_{21}$  related to the  $x_2$ -direction.

In a final parametric study, the effects of variations in the expectation value  $\mathcal{E}(s_\vartheta)$  and the standard deviation  $\mathcal{S}(s_\vartheta)$  of the variability  $s_\vartheta$  of the out-of-plane fiber angle  $\vartheta$  (see Fig. 9) is investigated. The results are presented in Fig. 13. For geometric restrictions, i.e. fiber lengths in excess of the plate thickness, the possible ranges for the out-of-plane fiber angle  $\vartheta$  and thus its possible scatter are much smaller than for its in-plane counterpart  $\varphi$ . Consequently, the expectation value  $\mathcal{E}(s_\vartheta)$  and the standard deviation  $\mathcal{S}(s_\vartheta)$  for the parameter  $s_\vartheta$  can be varied only in much smaller ranges than for the parameter  $s_\varphi$  considered in Fig. 12. Due to the smaller variations in the input probability distributions, the observed variations in the probability distributions are also much smaller than for the in-plane fiber orientation scatter and parameter. Changes in the expectation value  $\mathcal{E}(s_\vartheta)$  of the out-of-plane fiber orientation scatter band parameter  $s_\vartheta$  result in shifts in the probability distributions for the effective material properties  $\bar{E}_i$ ,  $\bar{G}_{ij}$  and  $\bar{\nu}_{ij}$ . Due to the limited possible range for variation of the input probability distribution  $\mathcal{F}(s_\vartheta)$ , only limited effects on the probability distributions  $\mathcal{F}(\bar{E}_i)$ ,  $\mathcal{F}(\bar{G}_{ij})$  and  $\mathcal{F}(\bar{\nu}_{ij})$  are obtained. Regarding variations in the standard deviation  $\mathcal{S}(s_\vartheta)$  of the input probability distribution in the sensible range, the probability distributions for the effective properties  $\bar{E}_i$ ,  $\bar{G}_{ij}$  and  $\bar{\nu}_{ij}$  are found insensitive (see Figs. 13(b), (d) and (e)).

## 5 Conclusions

The present study has been concerned with an investigation into material uncertainty effects for long fiber reinforced thermoplastic materials (LFT). The material uncertainties derive from their disordered, uncertain microstructure which in addition is process and position dependent. In a preliminary experimental study, the local strain fields on the surfaces of macroscopic tensile specimens have been determined. The specimens were cut from the flow range of a plane PA66-GF40 plate and have been tested longitudinal and perpendicular to the fiber preference direction have been determined. The results reveal a distinct uncertainty in the elastic moduli  $\bar{E}_1$  and  $\bar{E}_2$  longitudinal and perpendicular to the fiber preference direction as well as for the in-plane Poisson's ratios  $\bar{\nu}_{21}$  and  $\bar{\nu}_{12}$ .

For a consideration of the uncertainty effects in the numerical simulation of the structural response of LFT structures and components, a probabilistic elasticity model is proposed. The model is based on the rules of mixture in conjunction with an ensemble averaging approach. In a probabilistic enhancement, the local fiber volume fraction together with the parameters controlling the probability density distributions of the two fiber angles in 3D space are treated as random variables, each provided with an appropriate probability distribution. The model is able to predict the probability distributions for the entire set of effective elastic properties together with their interrelations based on a minimum number of random variables.

The model is applied in a parametric study on the effective material response of the PA66-GF40 material investigated in the experimental study. For the numerical computation of the probability distributions for the effective elastic constants, a discretizing numerical scheme using a predefined discretization of the space of the random variables is utilized. The scheme proves to be reliable and numerically efficient. In a comparison of the numerical prediction with the experimental data, a rather good agreement is observed.

## Acknowledgement

The present work has partially been funded by the Deutsche Forschungsgemeinschaft (DFG, German Research Foundation) under grant no. Ho1852/6-2. The financial support is gratefully acknowledged.

## References

- [1] Altendorf, H., Jeulin, D. and Willot, F.: *Influence of the fiber geometry on the macroscopic elastic and thermal properties*, Int. J. Solids Struct. **51** (2014) 3807-3822.
- [2] Beckmann, C. and Hohe, J.: *Numerical prediction of disorder effects in solid foams using a probabilistic homogenization scheme*, Mech. Mat. **78** (2014) 22-43.
- [3] Bednarczyk, B., Aboudi, J. and Arnold, S.M.: *The effect of general statistical fiber misalignment on predicted damage initiation in composites*, Compos. B **66** (2014) 97-108.
- [4] Bijsterbosch, H. and Gaymans, R.J.: *Polyamide 6 - long glass fiber injection moldings*, Polymer Compos. **16** (1995) 363-369.
- [5] Dirrenberger, J., Forest, S. and Jeulin, D.: *Towards gigantic RVE sizes for 3D stochastic fibrous networks*, Int. J. Solids Struct. **51** (2014) 359-376.
- [6] Dunn, M.L., Ledbetter, H., Heylinger, P.R. and Choi, C.S.: *Elastic constants of textured short-fiber composites*, J. Mech. Phys. Solids **44** (1996) 1509-1541.
- [7] Eshelby, J.D.: *The determination of the elastic field of an ellipsoidal inclusion, and related problems*, Proc. Roy. Soc. A **241** (1957) 376-396.
- [8] Fliegner, S., Luke, M. and Gumbsch, P.: *3D microstructure modeling of long fiber reinforced thermoplastics*, Compos. Sci. Tech. **104** (2014) 136-145.
- [9] Fu, S.Y. and Lauke, B.: *Effects of fiber length and fiber orientation distributions on the tensile strength of short-fiber-reinforced polymers*, Compos. Sci. Tech. **56** (1996) 1179-1190.
- [10] Garesci, F. and Fliegner, S.: *Young's modulus prediction of long fiber reinforced thermoplastics*, Compos. Sci. Tech. **85** (2013) 142-147.

- [11] Halpin, J.C. and Kardos, J.L.: *The Halpin-Tsai equations – a review*, Polym. Eng. Sci. **16** (1976) 344-352.
- [12] Henning, F., Ernst, H., Brüssel, R., Geiger, O. and Krause, W.: *LFTs for automotive applications*, Reinf. Plastics **49** (2005) 24-33.
- [13] Hill, R.: *A self-consistent mechanics of composite materials*, J. Mech. Phys. Solids **13** (1965) 213-222.
- [14] Hohe, J. and Beckmann, C.: *Probabilistic homogenization of solid foams*. Proc. Appl. Math. Mech. **11** (2011) 527-528.
- [15] Hohe, J., Beckmann, C. and Paul, H.: *Modelling of uncertainties in long fiber reinforced thermoplastics*, Mat. Des. **66** (2015) 390-399.
- [16] Kunc, V., Case, S.W., Santos-Villalobos, H.J. and Simunovic, S.: *The stiffness tensor for composites with curved discontinuous fibers*, Compos. A **72** (2015) 239-248.
- [17] Lee, Y. and Jasiuk, I.: *Apparent elastic properties of random fiber networks*, Comput. Mat. Sci. **79** (2013) 715-723.
- [18] Lusti, H.R., Hine, P.J. and Gusev, A.A.: *Direct numerical predictions for the elastic and thermoelastic properties of short fibre composites*, Compos. Sci. Tech. **62** (2002) 1927-1934.
- [19] Ma, J., Zhang, S., Wriggers, P., Gao, W. and De Lorenzis, K.: *Stochastic homogenized effective properties of three-dimensional composite material with full randomness and correlation in the microstructure*, Comput. Struct. **144** (2014) 62-74.
- [20] Mesogitis, T.S., Skordos, A.A. and Long, A.C.: *Uncertainty in the manufacturing of fibrous thermosetting composites: A review*, Compos. A **57** (2014) 67-75.
- [21] Mori, T. and Tanaka, K.: *Average stress in matrix and average elastic energy of materials with misfitting inclusions*, Acta Metall. **21** (1973) 571-574.
- [22] Nguyen, B.N. and Khaleel, M.A.: *A mechanistic approach to damage in short-fiber composites based on micromechanical and continuum damage mechanics descriptions*, Compos. Sci. Tech. **64** (2004) 607-617.
- [23] Phelps, J.H., Abd El-Rahman, A.I., Kunc, V. and Tucker, C.L.: *A model for fiber length attrition in injection-moulded long-fiber composites*, Compos. A **51** (2013) 11-21.
- [24] Rahman, S. and Chakraborty, A.: *A stochastic micromechanical model for elastic properties of functionally graded materials*, Mech. Mat. **39** (2007) 548-563.
- [25] Sakata, S. and Torigoe, I.: *A successive perturbation-based multiscale stochastic analysis method for composite materials*, Fin. Elem. Anal. Des. **102-103** (2015) 74-84.
- [26] Sharma, B.N., Kijewski, S.A., Fifield, F., Shin, Y., Tucker, C.L. and Sangid, M.D.: *Reliability in the characterization of fiber length distributions of injection molded long carbon fiber composites*, Polym. Compos. (in press).
- [27] Sharma, B.N., Naragani, D., Nguyen, B.N., Tucker, C.L. and Sangid, M.D.: *Uncertainty quantification of fiber orientation distribution measurements for long-fiber-reinforced thermoplastic composites*, J. Compos. Mat. (in press).
- [28] Soize, C.: *Non-Gaussian positive-definite matrix-valued random fields for elliptic stochastic partial differential operators*, Comput. Meth. Appl. Mech. Eng. **195** (2006) 26-64.
- [29] Sriramula, S. and Chryssanthopoulos, M.K.: *Quantification of uncertainty modelling in stochastic analysis of FRP composites*, Compos. A **40** (2009) 1673-1684.
- [30] Taya, M. and Chou, T.W.: *Prediction of the stress-strain curve of a short-fibre reinforced thermoplastic*, J. Mat. Sci. **17** (1982) 2801-2808.

- [31] Thieme, M., Böhm, R., Gude, M. and Hufenbach, W.: *Probabilistic failure simulation of glass fibre reinforced weft-knitted thermoplastics*, Compos. Sci. Tech. **90** (2014) 25-31.
- [32] Thomason, J.L.: *The influence of fibre length and concentration on the properties of glass fibre reinforced polypropylene: 5. Injection moulded long and short fibre PP*, Compos. A **33** (2002) 1641-1652.

## List of Figures

1	Direct LFT process and test plate. . . . .	18
2	Specimen geometry and positions for local evaluation. . . . .	18
3	Engineering stress-strain curves and failure modes. . . . .	19
4	Local strain fields (longitudinal engineering strain, specimen P3-S-0°). . . . .	19
5	Envelopes for local longitudinal strains – experimental results (0.9 mm × 0.9 mm). . . . .	20
6	Probability distributions for local longitudinal strains – experimental results. . . . .	21
7	Probability distributions for the longitudinal elastic moduli – experimental results. . . . .	22
8	Probability distributions for the in-plane Poisson’s ratios – experimental results. . . . .	22
9	Representative volume element and coordinate systems. . . . .	23
10	Discretization of the space of the random variables. . . . .	23
11	Effect of uncertainties in the fiber volume fraction. . . . .	24
12	Effect of uncertainties in the in-plane fiber orientation scatter band parameter. . . . .	25
13	Effect of uncertainties in the transverse fiber orientation scatter band parameter. . . . .	26

## List of Tables

1	Macroscopic experimental results. . . . .	26
---	-------------------------------------------	----

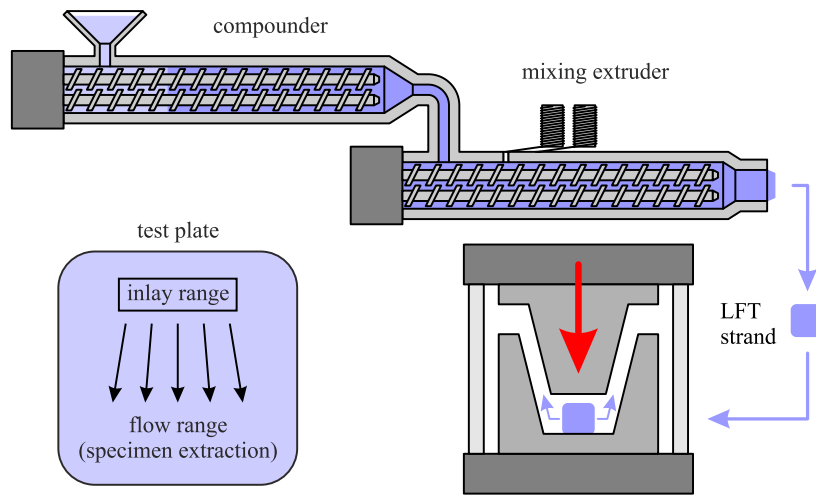


Figure 1: Direct LFT process and test plate.

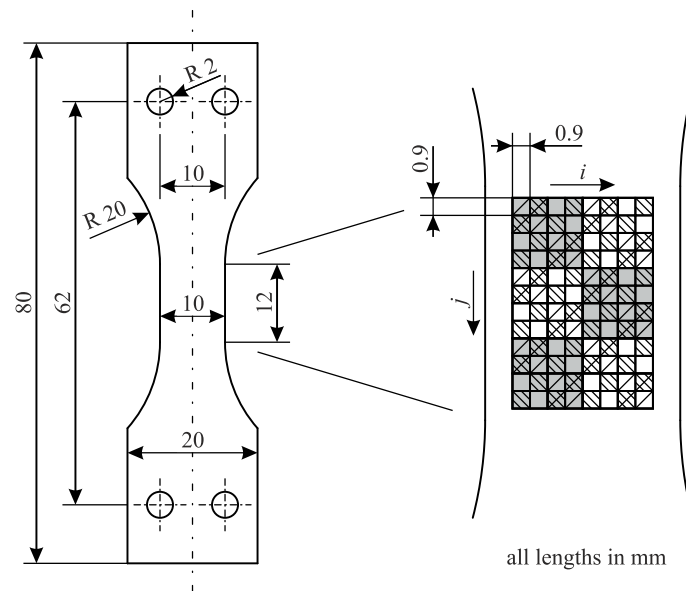


Figure 2: Specimen geometry and positions for local evaluation.

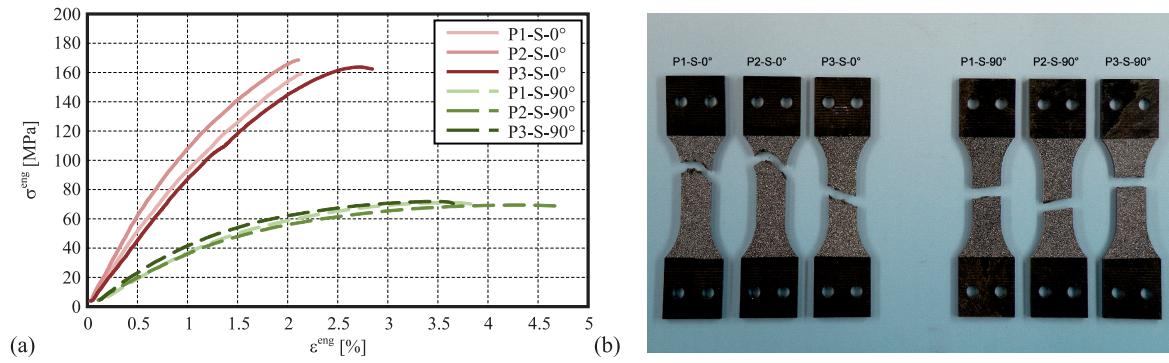


Figure 3: Engineering stress-strain curves and failure modes.

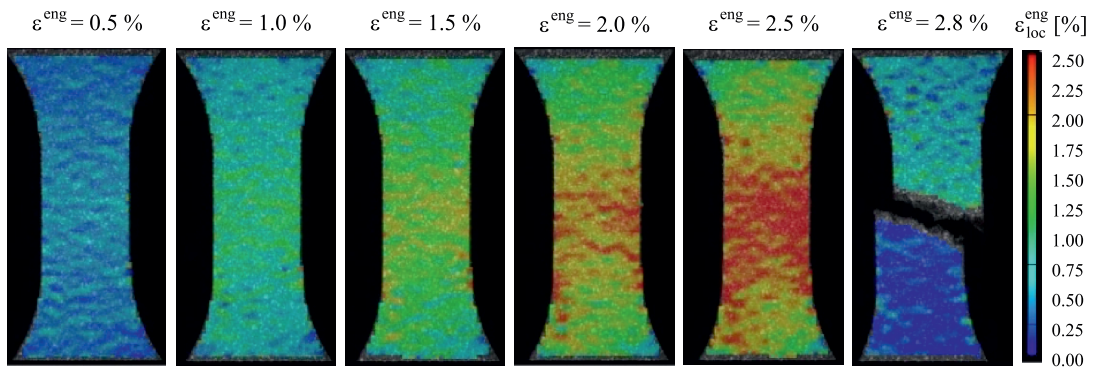


Figure 4: Local strain fields (longitudinal engineering strain, specimen P3-S-0°).

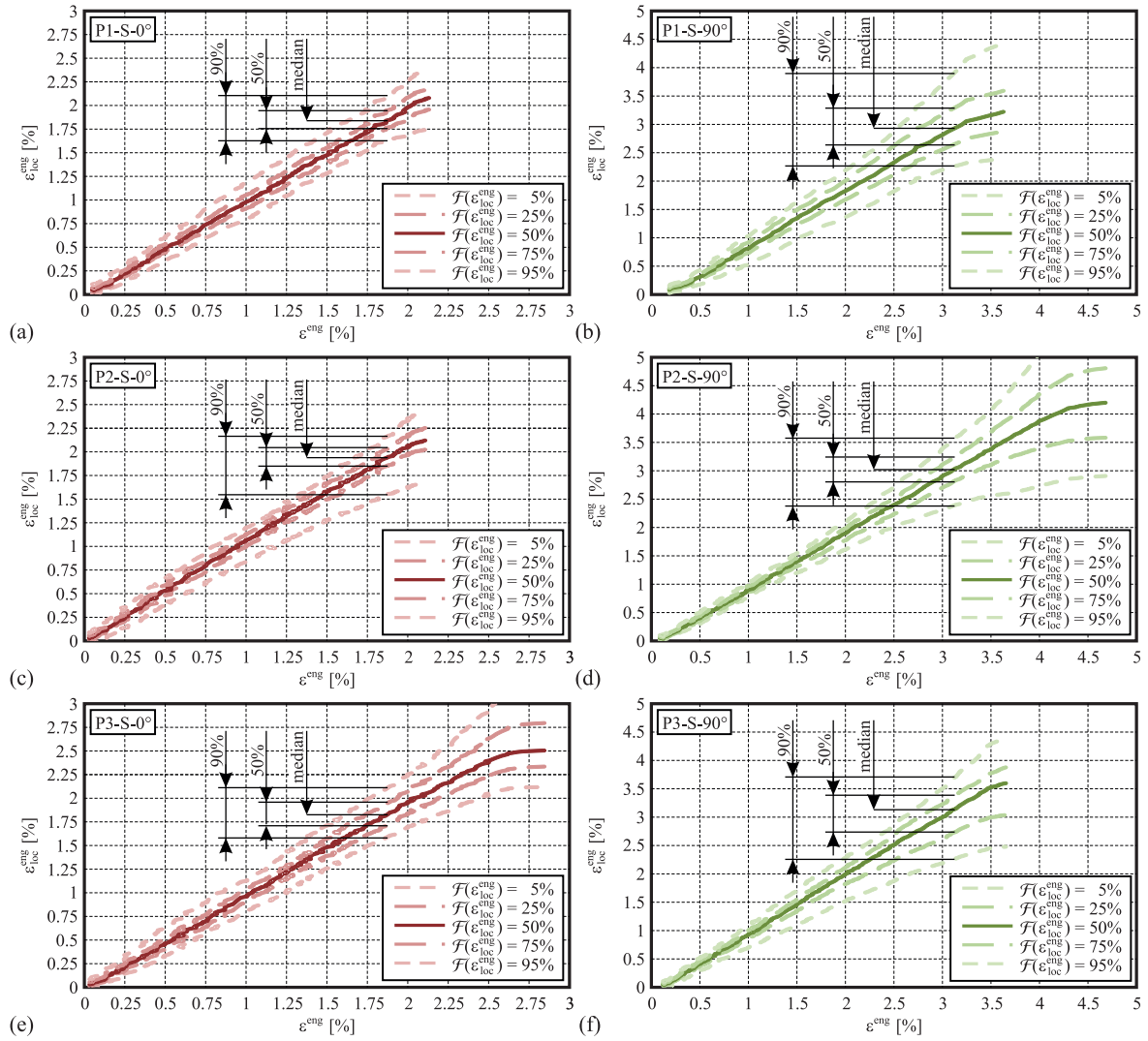


Figure 5: Envelopes for local longitudinal strains – experimental results (0.9 mm × 0.9 mm).

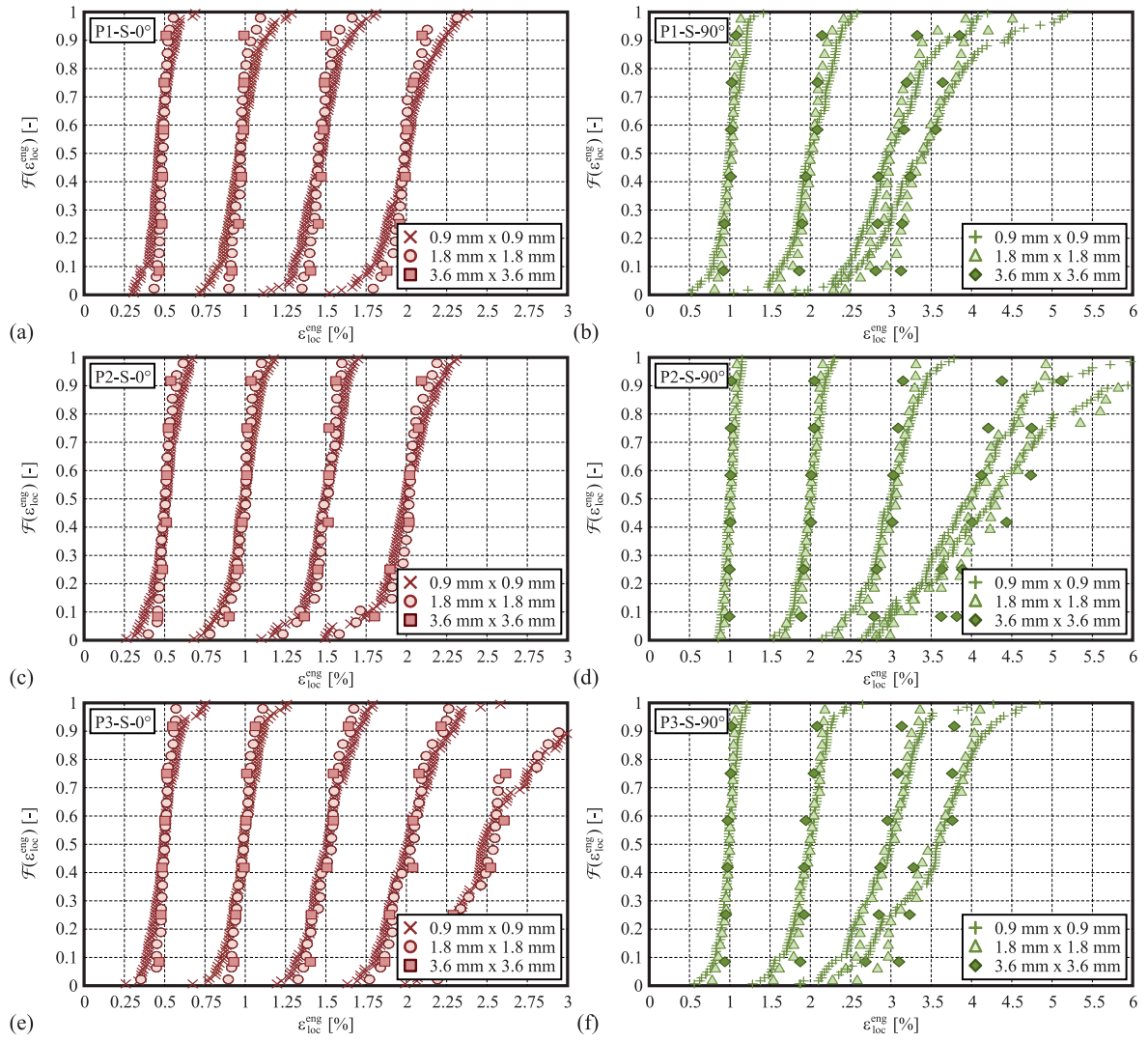


Figure 6: Probability distributions for local longitudinal strains – experimental results.

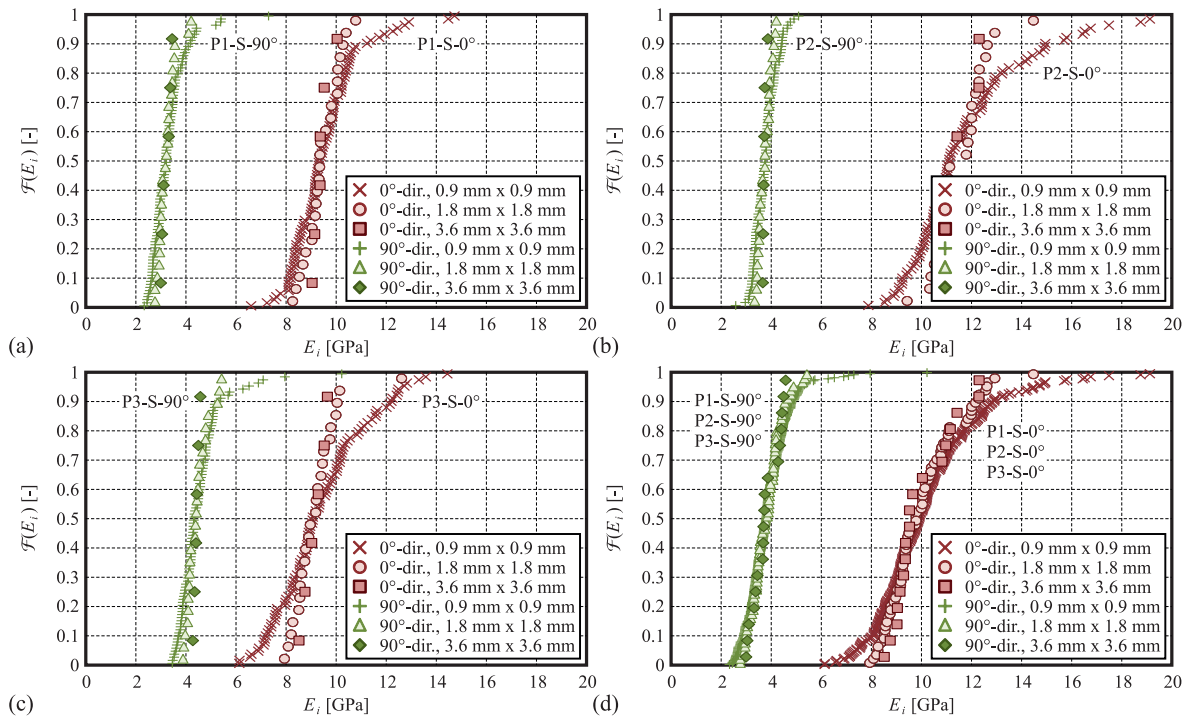


Figure 7: Probability distributions for the longitudinal elastic moduli – experimental results.

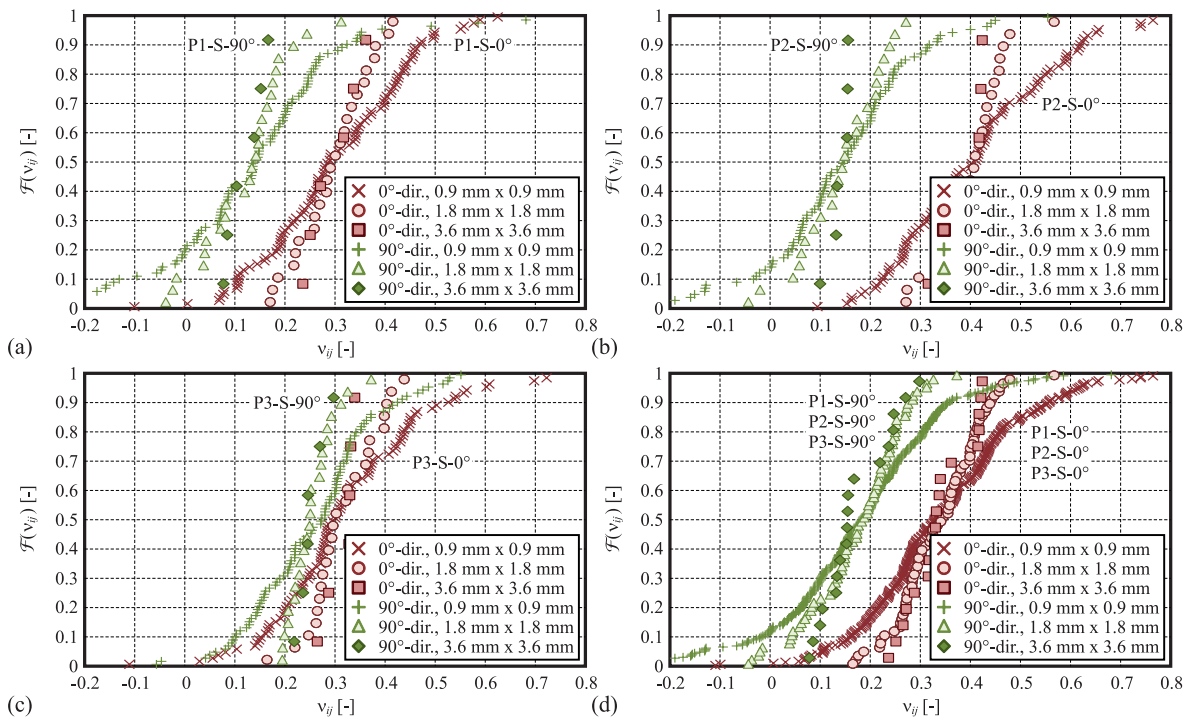


Figure 8: Probability distributions for the in-plane Poisson's ratios – experimental results.

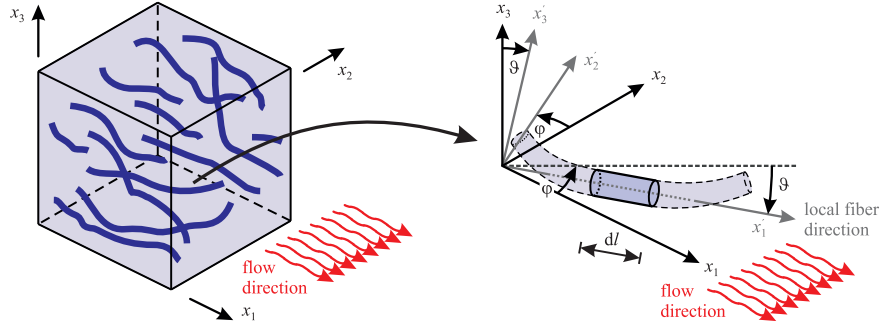


Figure 9: Representative volume element and coordinate systems.

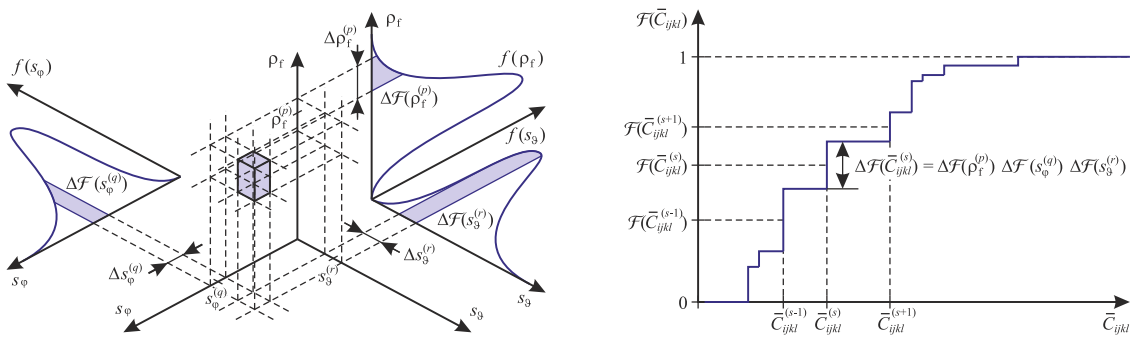


Figure 10: Discretization of the space of the random variables.

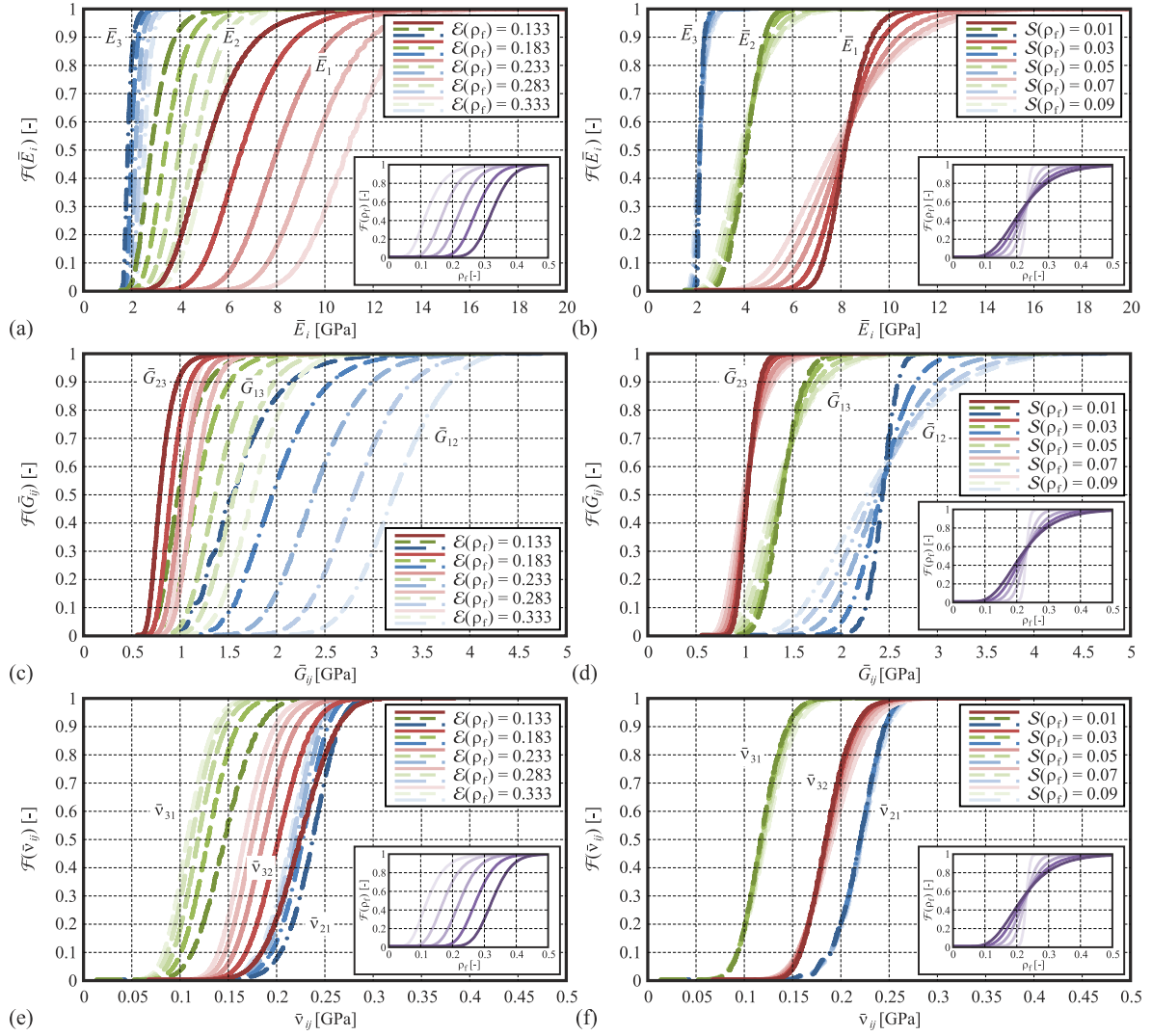


Figure 11: Effect of uncertainties in the fiber volume fraction.

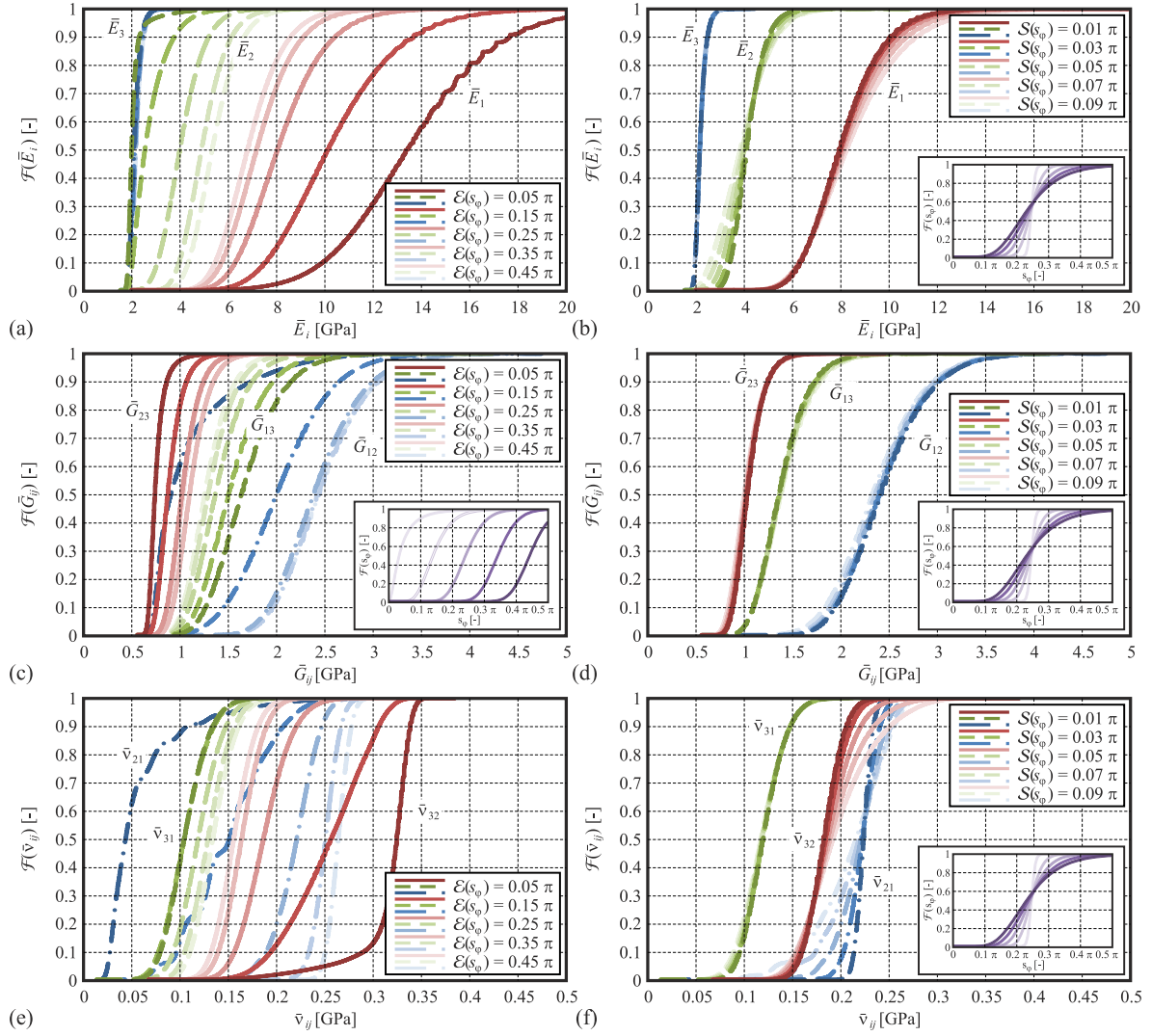


Figure 12: Effect of uncertainties in the in-plane fiber orientation scatter band parameter.

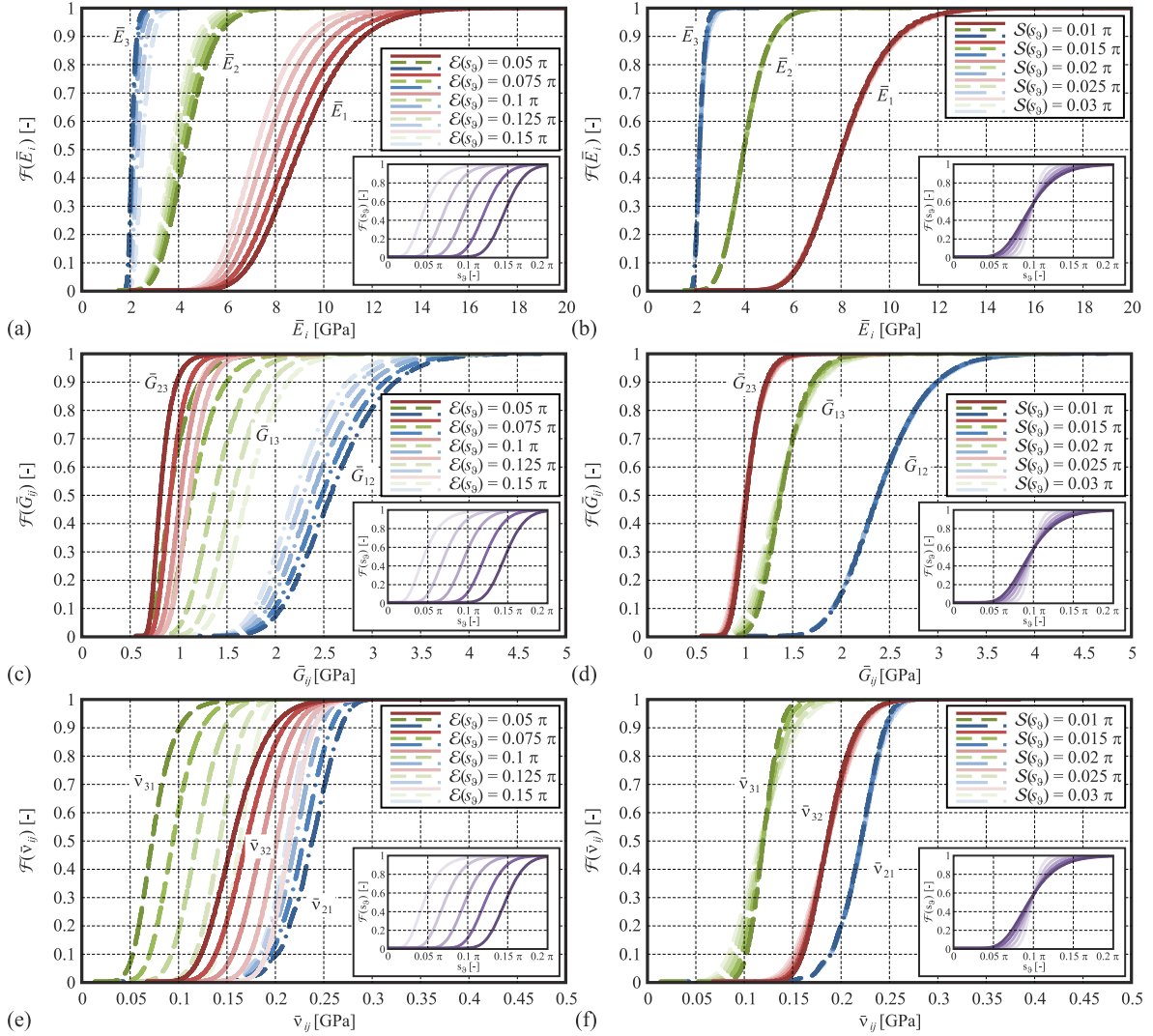


Figure 13: Effect of uncertainties in the transverse fiber orientation scatter band parameter.

Table 1: Macroscopic experimental results.

longitudinal to flow direction			transversal to flow direction		
specimen no.	$E_1$	$R_m$	specimen no.	$E_2$	$R_m$
[-]	[GPa]	[MPa]	[-]	[GPa]	[MPa]
P1-S-0°	10.067	158.97	P1-S-90°	3.243	71.04
P2-S-0°	12.890	168.55	P2-S-90°	3.685	69.39
P3-S-0°	8.613	163.74	P3-S-90°	4.587	71.83
expectation value $\mathcal{E}$	10.523	163.75	expectation value $\mathcal{E}$	3.838	70.76
standard deviation $\mathcal{S}$	2.175	4.79	standard deviation $\mathcal{S}$	0.685	1.25
variability $\mathcal{S}/\mathcal{E}$ [%]	20.668	2.93	variability $\mathcal{S}/\mathcal{E}$ [%]	17.849	1.76